ČESKÉ VYSOKÉ UČENÍ TECHNICKÉ V PRAZE
Fakulta jaderná a fyzikálně inženýrská

DIPLOMOVÁ PRÁCE

2014 Karol Ješko

ČESKÉ VYSOKÉ UČENÍ TECHNICKÉ V PRAZE
Fakulta jaderná a fyzikálně inženýrská
Katedra fyziky

DIPLOMOVÁ PRÁCE

Model rozdělovací funkce rychlostí elektronů plazmatu v blízkosti divertorových desek tokamaku JET

Model of electron velocity distribution function of JET divertor target plasmas

Posluchač: Karol Ješko
Školitel: Ing. Ivan Ďuran, Ph.D.
Akademický rok: 2013/2014

sem pride original zadania

Čestné prohlášení

Prohlašuji na tomto místě, že jsem předloženou práci vypracoval samostatně a že jsem uvedl veškerou použitou literaturu.

Nemám závažný důvod proti užití tohto školního díla ve smyslu §60 Zákona č. 121/2000 Sb., o právu autorském, o právech souvisejících s právem autorským a o změně něktrerých zákonů (autorský zákon).

V Praze dne 5. května 2014 ....

Karol Ješko

Poďakovanie

Ďakujem Ing. Ivanovi Ďuranovi, Ph.D. za trpezlivé vedenie diplomovej práce a za mnoho užitočných rád a návrhov, ktoré ju obohatili.

Název práce: **Model elektronové rozdělovací funkce rýchlosti elektronů v blízkosti divertorových desek tokamaku JET**

Autor: Karol Ješko

Obor: Fyzika a technika termojaderné fúze

Druh práce: Diplomová práce

Vedoucí práce: Ing. Ivan Ďuran, Ph.D., Ústav fyziky plazmatu AV ČR, v. v. i.

Abstrakt: Táto práca priamo nadväzuje na a rozširuje moju bakalársku prácu [11]. V úvodných kapitolách obsahuje základy termojadrovej fúzie a magnetického udržania. V ďalších kapitolách je popis fyziky scrape-off layer tokamaku a základné principy fungovania Langmuirovych sond. Hlavná časť práce spočíva v ďalšom vývoji modelu, ktorého úloha je určiť vplyv rýchlych elektrónov zo scrape-off layer na divertorové Langmuirove sondy a objasniť tým notorický problém nadhodnocovania elektrónovej teploty sondami pri vysokých hustotách v scrape-off layer. Model konštruuje elektrónovú rozdeľovaciu funkciu rýchlosti elektrónov pri divertore z ktorej sa určí voltampérová charakteristika divertorovej Langmuirovej sondy a tým pádom aj elektrónová teplota. V tejto práci sú prezentované doterajšie výsledky simulácií pre tokamak JET. V závere práce je systematické porovnanie výsledkov simulácií so skutočnými meraniami divertorových sond na JETe a porovnanie výslednej rozdeľovacej funkcie s PIC kódom BIT1.

Klíčová slova: JET, Scrape-off layer, Divertor, Langmuirova sonda, Elektrónová teplota
Title: **Electron velocity distribution function of JET divertor plasmas**

Author: Karol Ješko

Abstract: This thesis follows and expands my bachelors thesis [11]. In the beginning, a basics of thermonuclear fusion and magnetic confinement are given. In subsequen chapters, basic scrape-off layer physics is described and the principles of operation of Langmuir probes are introduced. The principal part of the thesis is about the further development of a simple model which aims at estimating the effect of suprathermal electrons originating in the SOL on divertor Langmuir probes and thereby clarify the problem of probe T_e overestimation for high densities in the SOL. The model calculates the electron velocity distribution function (EVDF) at the divertor. Using the EVDF, the probe IV characteristic and T_e can be calculated. In this thesis, results of simulations for tokamaks JET are presented. In the case of JET, a systematic comparison of simulation results with experimental divertor LP data is done and a benchmark of the model against the BIT1 PIC code is presented.

Key words: JET, Scrape-off layer, Divertor, Langmuir probe, Electron temperature

Contents

Chapter 1

Nuclear Fusion

1.1 Fusion reactions

The primary source of energy in the universe is the energy produced by stars. The stars produce their energy via a chain of thermonuclear fusion reactions identified in 1938 by Hans Bethe and independently by Carl Friedrich von Weizsäcker. This sequence of reactions is known as the carbon cycle. However, for smaller stars with lower central temperatures like our Sun, the proton-proton cycle dominates:

$$ {}_1\mathrm{H}^1 + {}_1\mathrm{H}^1 \longrightarrow {}_1\mathrm{D}^2 + \mathrm{e}^+ + \nu + 1.44\mathrm{MeV} \tag{1.1} $$

$$ {}_1\mathrm{D}^2 + {}_1\mathrm{H}^1 \longrightarrow {}_2\mathrm{He}^3 + \gamma + 5.49\mathrm{MeV} \tag{1.2} $$

$$ {}_2\mathrm{He}^3 + {}_2\mathrm{He}^3 \longrightarrow {}_2\mathrm{He}^4 + \mathrm{e}^+ 2{}_1\mathrm{H}^1 + 12.86\mathrm{MeV} \tag{1.3} $$

where e^+, ν and γ are a positron, neutrino and gamma-ray, respectively. The energy released per reaction is also depicted. The third reaction in this cycle only takes place when the temperature is above 10^7 K but comprises almost half of the total energy releas of the p-p cycle. This energy provides stellar stability that prevents gravitational collapse of the star and determines the physics of the star in outer layers as well.

Fusion reactions that are more suitable for controlled thermonuclear fusion are the following:

$$ {}_1\mathrm{D}^2 + {}_1\mathrm{T}^3 \longrightarrow {}_2\mathrm{He}^4 + {}_0\mathrm{n}^1 + 17.6\mathrm{MeV} \tag{1.4} $$

$$ {}_1\mathrm{D}^2 + {}_1\mathrm{D}^2 \longrightarrow {}_2\mathrm{He}^3 + {}_0\mathrm{n}^1 + 3.27\mathrm{MeV} \tag{1.5} $$

$$ {}_1\mathrm{D}^2 + {}_1\mathrm{D}^2 \longrightarrow {}_1\mathrm{T}^3 + {}_1\mathrm{H}^1 + 4.03\mathrm{MeV} \tag{1.6} $$

$$ {}_1\mathrm{D}^2 + {}_2\mathrm{He}^3 \longrightarrow {}_2\mathrm{He}^4 + {}_1\mathrm{H}^1 + 18.3\mathrm{MeV} \tag{1.7} $$

By far the most promising of these alternatives is reaction 1.4. This can be inferred from Fig. 1.1, where the D-T reaction has the highest reaction rate for a temperature around 40 keV.

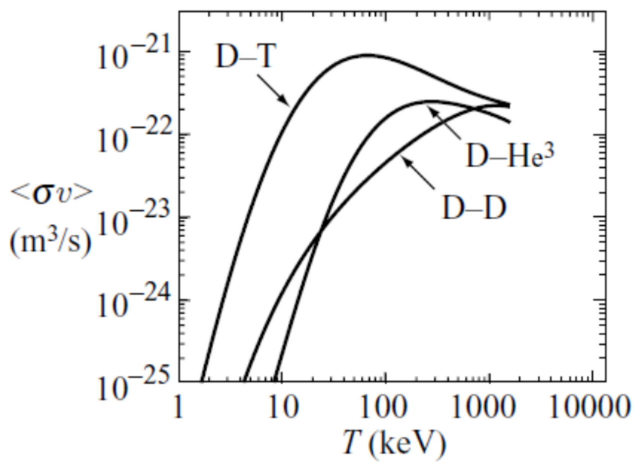

Figure 1.1: The reaction rate $\langle \sigma v \rangle$ as a function of the temperature for reactions 1.4-1.7. The D-D reaction rate is the sum of both branches of the reaction 1.5 and 1.6 [1].

The total energy output of 17.6 MeV is distributed between the alpha particle which has a kinetic energy of about 3.5 MeV and the neutron which carries the rest of the energy released. This reaction is foreseen to take place in future thermonuclear reactors.

1.2 Lawson criterion

A simple and widely used index of thermonuclear gain is provided by the Lawson criterion. Consider a thermonuclear reactor with equal densities of D and T fusion fuel, $n_{\mathrm{D}} = n_{\mathrm{T}} = n/2$. The thermonuclear fusion power generated in a thermonuclear reactor (per unit volume) is

$$P_{\mathrm{fus}} = \frac{1}{4} n^2 \langle \sigma v \rangle \Delta E \tag{1.8}$$

where $\langle \sigma v \rangle$ denotes the reaction rate, σ being the collisional cross-section for fusion and v is the relative velocity of colliding particles.

From momentum conservation, $1/5$ of this output power is carried by the α-particles, while the rest is carried by neutrons which escape from the reactor. Thus the heat added to unit volume of plasma per unit time as a result of fusion is $P_\alpha = \frac{1}{4} n^2 \langle \sigma v \rangle E_\alpha$, where $E_\alpha = 3.5$ MeV is the energy corresponding to the α particle created in one reaction.

Now let us consider the energy lost from the fusion plasma. First, let us account for radiation loss, arising in particular from bremstrahlung due to electron-ion collisions.

From [34], the formula for bremsstrahlung power loss from a hot plasma can be written (per unit volume) as

$$P_{\mathrm{b}} = \beta n^2 T^{1/2}, \tag{1.9}$$

where β is a constant and T is the plasma temperature.

Energy losses of other types (heat lost to the wall surrounding the plasma by conduction and convection) is expressed to happen at a rate $3nkT/\tau_{\mathrm{E}}$, where τ_{E} is the energy confinement time.

Balancing power gain against loss we arrive at a relation for $n\tau$. The *Lawson criterion* for power can then be expressed

$$n\tau = \frac{3kT}{\frac{1}{4}\langle\sigma v\rangle E_{\alpha} - \beta T^{1/2}}. \tag{1.10}$$

Thus for ignition, the product of density and confinement time must be equal to the right hand side, which is a function of the temperature. In Fig. 1.2 one can see that the temperature function on the right hand side has a minimum for T=30 keV, where for ignition, $n\tau = 10^{20}$ m^{-3}s.

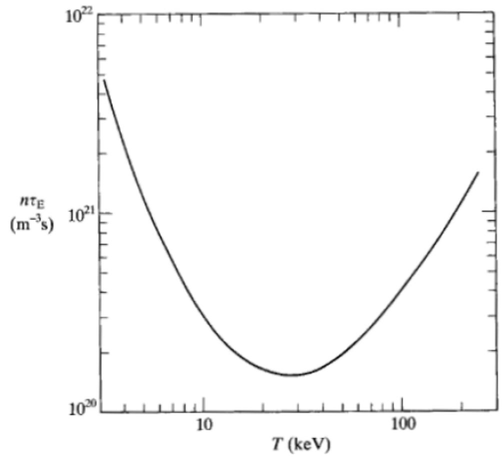

Figure 1.2: The Lawson criterion for ignition of fusion reactions. [1].

1.3 Magnetic confinement

A possibility to confine a hot thermonuclear plasma in a given space is by using magnetic fields. Early devices such as Z-pinches, while containing and pinching the plasma radially, suffered serious losses at the ends of the device. Other approaches trapped the plasma in a magnetic bottle (mirror machine) or used a closed toroidal vessel. Of the latter the tokamak, an abbreviation of the Russian for toroidal magnetic chamber, has been the most successful.

The magnetic field of a tokamak is defined by two components:

- A strong toroidal field generated by external currents in toroidal field coils.

- A poloidal field generated by the plasma current, which is induced by the central solenoid.

The poloidal field is typically an order of magnitude smaller than the toroidal field. The resulting field is a helical field. Figure 1.3 illustrates the tokamak configuration.

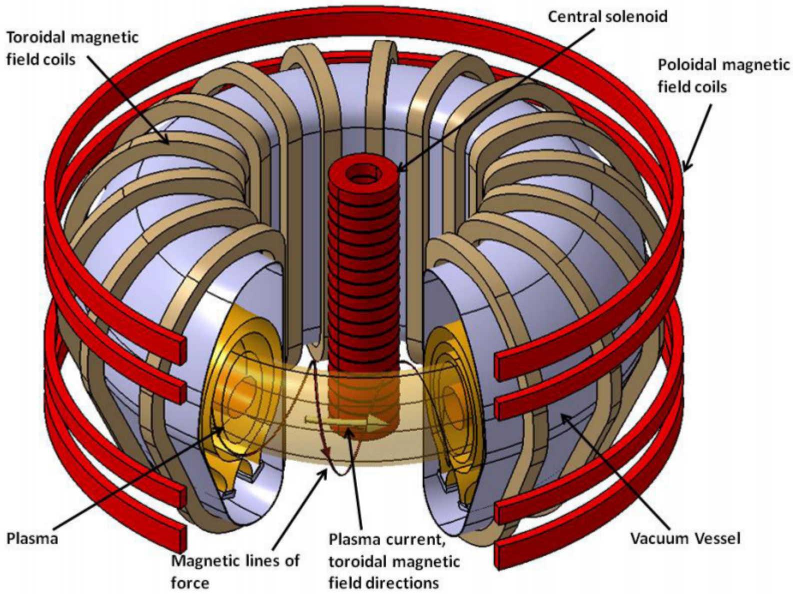

Figure 1.3: Illustration of the tokamak configuration [10].

A plasma in a purely toroidal field drifts towards the outer wall. This drift may be countered by balancing the outward force with the magnetic pressure from the poloidal field, produced by the plasma current. For a typical tokamak plasma density the Lawson criterion requires energy confinement times of a few seconds.

The poloidal field coils depicted in the Fig. 1.3 stabilize the plasma position and are also used to for plasma shaping. Additionally, poloidal field coils are also utilized to create the divertor configuration, described in section 2.1.2.

1.4 The Joint European Torus

A number of relatively succesfull early tokamaks like T-3[1], ST[2] and TFR[3] provided the encouragement to make a big step towards a reactor concept. Europe agreed to pursue this goal by setting up a large scale collaborative project, the Joint European Torus - JET.

[1] T-3 resulted from the Soviet tokamak programme in the 1960s, with temperatures of 1000 eV achieved.

[2] ST-Stellarator tokamak, located at Princeton Plasma Physics Laboratory, was originally a stellarator later converted into a tokamak. Here, high achievable temperatures were confirmed, however a new MHD instability, the sawtooth instability, was recognized.

[3] TFR-Tokamak de Fontenay aux Roses, located in a suburb of Paris, started operation in 1973. Temperatures of 2-3 keV were achieved, solely in Ohmic regimes.

The JET tokamak has a major radius of 2.96 m and minor radii 2.10 m in the vertical direction and 1.25 m in the horizontal direction.This makes it the largest operating tokamak to date. Plasma currents up to 5 MA and pulse lenghts up to 60 seconds can be achieved.

1.4.1 Vacuum vessel

The main purpose of the vacuum vessel is to hold a vacuum with the pressure of the orders of 10^{-2} Pa. Next, the vessel can be baked to clean the plasma-facing surface of the vessel from impurities by baking at temperatures $\sim$500 °C. Thus, this requires that the heating and cooling of the structure is not overloaded by stresses that are too large. A double skin was adapted for the vessel, through which hot gas can pass to heat it.

The thickness of the material needed to sustain the stresses mentioned above would imply low electric resistance of the structure. Consequently, current driving field would also induce a large current in the vessel itself. This matter is solved by alternating the strong metal section of the vessel with sections with high resistance. The nickel alloy construction of the vessel thus needed eight kilometres of vacuum tight welds to connect the sections.

1.4.2 Field coils

The toroidal field is created by 32 D-shaped coils enclosing the vacuum vessel [2], each weighing 12 tonnes, Fig. 1.4(a). Forces acting on the coils are compensated by an outer mechanical structure. The structure is illustrated in Fig.1.4(b).

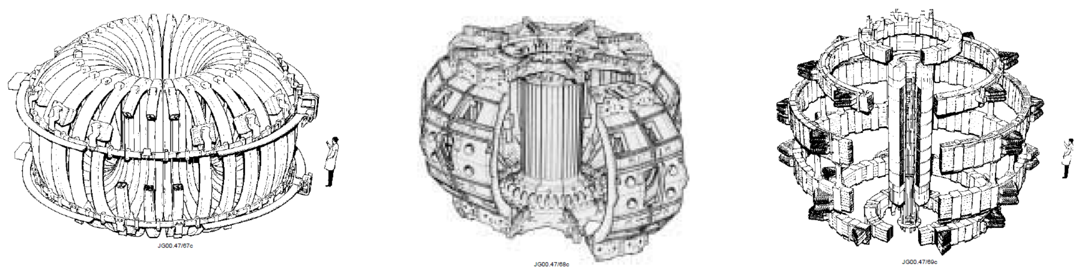

(a) (b) (c)

Figure 1.4: Layout of the toroidal field coils (a), support structure (b), poloidal field coils (c). [2]

Poloidal field coils have the shape of horizontal circular coils. They are placed outside the toroidal field coils and are illustrated in Fig. 1.4(c). The most important poloidal coil is the central solenoid which is wounded around the central column of an iron tranformer core, used to generate the flux swing to induce the plasma current. The other coils, six in total, are used to shape the plasma ring and control its position.

The transformer core would envelope all the components and with a weight of 2600 tonnes would dominate the appearance of JET.

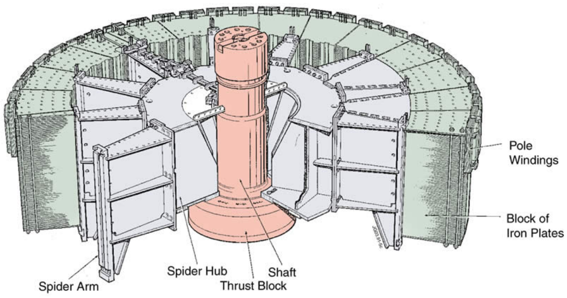

Figure 1.5: A sectional view of the flywheel rotor. [5]

1.4.3 Power supplies

Electrical power is needed to supply the currents in both the toroidal and poloidal field coils. Approximately a similar power is required for each. Additional power is needed to supply the heating systems. JET was designed to allow a pulse repetition rate of one every 15 minutes. Each pulse calls for a total power of hundreds of MW - which is in the range of the electrical output power of a standard commercial fission reactor. In total, JET's power supply system has an installed capacity approaching 1400 megawatt [5]. Uniquely, part of this power is provided directly from the electric grid (up to 575 MW). The remaining power is supplied by two massive 400 MW flywheels. The rotating part of each generator is 9 metres in diameter and weighs 775 tons, much of which is concentrated on the rim to form a large flywheel.

1.4.4 Heating

In the initial phase of a tokamak discharge, the plasma is Ohmically heated by the toroidal current. However, with increasing temperature the resistivity of the plasma falls. Therefore it can be stated that the Ohmic heating is self-limiting. For thermonuclear temperatures, Ohmic heating can not be counted on.

One type of auxiliary heating at JET is neutral beam injection. As of 2014, there are two neutral injector boxes (NIB), located at Octant 4 and 8. Each of the NIBs can house up to 8 positive ion neutral injectors (PINIs). Four PINIs on each NIB are accomodated in two banks:

- Normal bank - One pass through the plasma.
- Tangential bank - Two passes through the plasma. See Fig. 1.7

The whole neutral beam system is designed to provide maximum heating power of 25 MW during 10 seconds [4].

Another method of heating the tokamak plasma are high frequency electromagnetic waves. The antennae are placed in the limiter shade to prevent high heat fluxes and their melting. The rapidly oscillating electric field is set to a frequency which is in resonance with a characteristic frequency of the plasma (eg. cyclotron frequency)

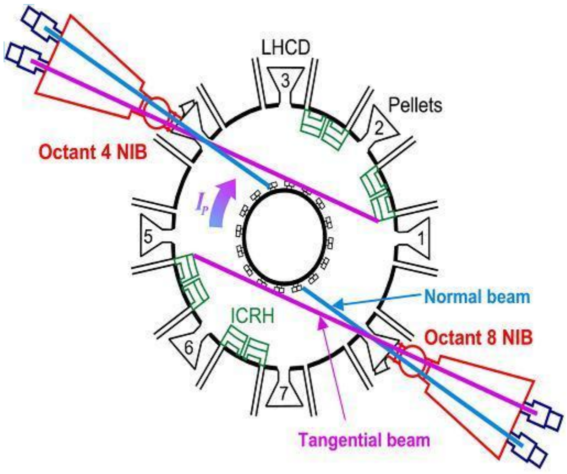

Figure 1.6: JET neutral beam system layout. [4]

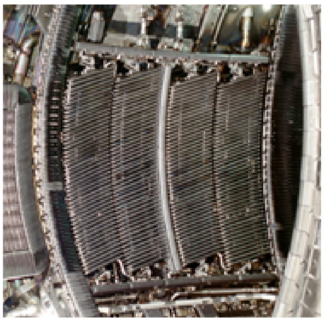

Figure 1.7: A photo of the new ITER-like ICRH antenna. [4]

and this accelerates the particles to a higher energy. A number of heating schemes exist, and either the ions or electrons can be heated, depending on the heating scheme. JET uses two distinct resonant frequencies:

- Ion cyclotron resonance resonance frequency (ICRH).
- Lower hybrid frequency (LH).

Chapter 2

Physics of the tokamak scrape-off layer

This chapter deals with the complex issues of the tokamak scrape-off layer and plasma-wall interactions (PWIs). Understanding the mechanisms of PWIs and the ability to eliminate their negative effects on the plasma confinement, on the lifetime of surface materials etc. is crucial on the way to design a fusion reactor.

2.1 The scrape-off layer

In tokamaks, there are two basic configurations which define the scrape-off layer and thus localize the plasma-surface interactions.

2.1.1 Limiter configuration

The first configuration, known as the limiter configuration, defines the plasma-wall interaction by inserting a solid object into the tokamak vessel, called a limiter. They can have various forms. The most simple concept is a circular diaphragm perpendicular to the toroidal field. This is called a poloidal limiter. Other geometrical configurations are also possible, illustrated in Fig. 2.1. By introducing such a structure in the vessel, some magnetic field lines intersect the solid surface, while others remain closed within the plasma. This defines a last closed flux surface (LCFS). The region radially inside the LCFS is the main, core plasma while the one outside is called the *scrape-off layer* (SOL). Typically, particles entering the SOL from the main plasma terminate on the solid limiter surface.

2.1.2 Divertor configuration

The way a divertor configuration is realized is somewhat different. In this case, the LCFS is created by introducing a magnetic X-point into the poloidal magnetic field. This is done by driving currents through specific poloidal field coils. The simplest and most common case is to have one poloidal field coil placed under the vacuum vessel -

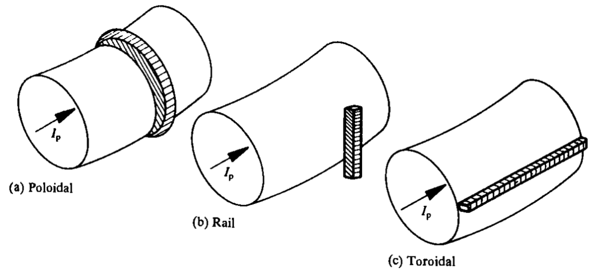

Figure 2.1: Several types of limiters [3]

this coil is often termed the divertor coil. For an X-point to form, the current in the poloidal field coils must have the same sign (direction) as the plasma current. Once the X-point is formed, the LCFS is given by the magnetic separatrix arising from this configuration. The place where the separatrix intersects the solid surface, usually a divertor target plate, is called the *strike point*. In a standard divertor configuration with one X-point, one has two strike points when looking at the poloidal cross section of the tokamak vessel, Fig. 2.2. This setup is schematically illustrated in Fig. 2.2. As in the limiter case, the area inside the separatrix, on close flux surfaces, is the main plasma, while the area situated radialy outboard, on "open" surfaces is the scrape off layer.

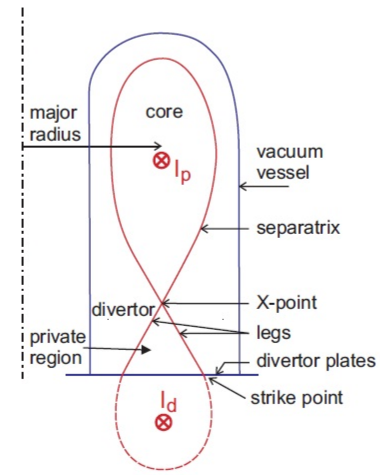

Figure 2.2: The setup of a divertor configuration [7]

2.2 PWIs relevant to tokamak plasmas

It is known from experiment, that the radial SOL width is small, in the order of a few centimeters, thus limiters and divertor targets experience high particle and heat fluxes, which cause the following:

2.2.1 Physical sputtering of the wall material

Energetic ions arriving at the material surface "knock out" neutral atoms from the lattice. Regarding the wall materials used (C, Mo, W), these neutral impurities have usually high atomic numbers. While the impurities penetrate further into the plasma, they undergoe the following inelastic collisions:

(a) Ionization - Neutral impurities undergoe ionization through their many charge states, which cools the plasma substantially.

(b) Atomic processes - Impurities and their charge states radiate line spectra, especially if the temperature gets low, further cooling the plasma.

Furthermore, sputtering gradually causes the walls to erode, which will be an issue once a reactor concept is needed.

There is a general threshold energy E_T for the incident ion below which unsufficient energy is transfered to the lattice atoms for them to overcome the surface binding energy. The theoretically calculated formula for this energy is

$$E_\mathrm{T} = \frac{E_\mathrm{s}}{\gamma_\mathrm{sp}(1-\gamma_\mathrm{sp})}, \tag{2.1}$$

where E_s is the sublimation energy of target atoms and factor $\gamma_\mathrm{sp} = m_1 m_2/(m_1 + m_2)^2$ [3]. Fig. 2.3 gives results from Monte-Carlo simulations of sputtering yields for various target materials. These simulations agree well with experimental data except for the carbon case, where no threshold energy value is visible, due to chemical effects occuring for low energies of incident ions. This will be discussed in the next section.

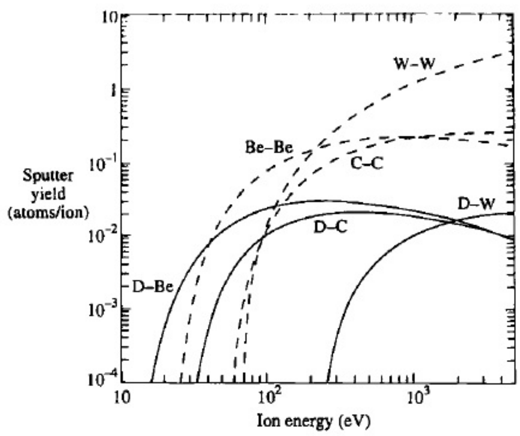

Figure 2.3: Sputtering yields by deuterium ions and self-sputtering yields as a function of the incident ion energies for Be, C, W. [Eckstein, W. Sputtering data, report PP9/82, Max Planck Institut fuer plasma physik, Garching, 1993], taken from [3].

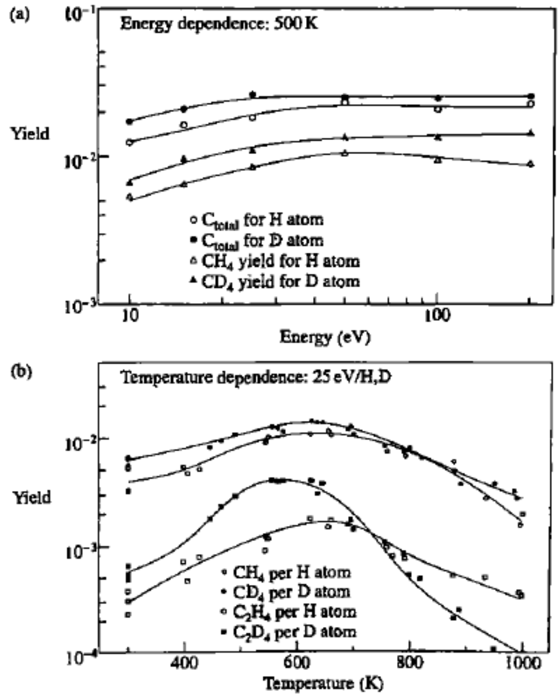

Figure 2.4: Chemical erosion yields of graphite bombarded by hydrogen and deuterium ions. (a) Energy dependance at fixed temperature 500K (b) Temperature dependance at fixed energy 25 eV. C_{total} refers to all sputtered hydrocarbons

2.2.2 Chemical sputtering of the wall materials

Sputtering caused by chemical reactions can be clearly identified in particular for low energies of the incident ions. Carbon is extensively used as a material for divertors because of its good refractory properties and the fact that it does not melt. For example, carbon tiles react with hydrogen (forming mainly CH_4, but also other hydrocarbons) and with oxygen (forming CO). Due to typically low binding energies of the products to the surface, products leave the surface easily at temperatures as low as 300 K [3], significantly contributing to the erosion of the material surface.

The dependance of chemical sputtering yields on incident ion energy at a fixed temperature and vice versa are shown in Fig. 2.4 (a) and (b) respectively. One can see that methane the most numerous hydrocarbon produced, but lesser amounts of ethylene (C_2H_4) and C_3H_6 are also produced. In contrary to physical sputtering, there is no threshold energy below which yields are zero and so chemical sputtering dominates for carbon when lower temperature plasmas are present.

2.2.3 Tritium retention

Tokamak walls contain a large concentration of gases. This issue can be illustrated by the example that in carbon, up to 0.4 H atoms (also D, T) can be implanted per one C atom. This is an issue especially for tritium. First, from the economical point of view, since tritium is not abundant in nature and must be manufactured. Second, high concentrations of tritium in the walls can be a radioactive hazard, since it decays by beta decay with a half-life of 12.32 years. The mechanism of tritium retention can be divided into two branches:

- **Implantation of plasma ions and charge exchange neutrals.** Ions are implanted where the field lines hit the solid. These implanted species thermalize in the lattice and diffuse in the direction opposite to the direction of the gradient of their concentration, until an equilibrium distribution is formed. Hydrogen isotopes have low diffusivity in carbon, resulting on high levels of trapped tritium. On the other hand, many metals have high diffusivity of hydrogen isotopes, leading to a reduced tritium inventory in the vacuum vessel. However, high diffusivity leads to permeation of the vacuum vessel. This can be eliminated by having a double vessel wall with a pumped interspace.

- **Co-deposition with the wall material in net redeposition regions.** Erosion in the high heat flux regions, resulting in impurity transport and redeposition elsewhere in the vessel tends to build up retained tritium levels. Unlike the first mechanism described, here, there is no saturation, the inventory builds up linearly, until the re-deposited layer reaches a thickness of about 10 μm. After this, the layer tends to exfoliate, resulting in the presence of radioactive dust in the vessel [3].

2.3 Divertor physics

2.3.1 Why divertors?

With regard to previous sections, the advantages of divertors over limiters can be summarized as follows:

- Keeping the plasma wall interactions remote from the main plasma.

- Better pumping of α-particles.

These advantages result in a cleaner, less diluted plasma and thus better confinement. It is also easier to achieve higher confinement mode (H-mode), on a tokamak with a divertor configuration.

On the other hand, the extremely expensive space given by the high vacuum and strong toroidal field should be filled with DT fuel as efficiently as possible. Regarding the divertors long legs that keep the PWI far from the core, it does not seem so advantageous in this sense.

Limiters still play an important role in divertor tokamaks in the initial phases of a discharge, when the plasma is circular. Additionally, limiters are used to protect RF antennae and they provide shade for a number of diagnostics.

Particles crossing the separatrix are quickly swept towards the divertor targets (or limiters, alternatively), i.e. parallel transport along the field lines dominates over radial (cross-field) transport. This leads to a radial density gradient in the SOL. The density in the SOL decays exponentially with a characteristic decay length λ_n^{SOL}:

$$n(r) = n_{\mathrm{LCFS}} \exp\left(-\frac{r}{\lambda_n^{\mathrm{SOL}}}\right). \tag{2.2}$$

This decay length is considered as the SOL width and can be experimentally determined by measuring the radial density profile in the SOL, by a reciprocating Langmuir probe, for example. It is expected that λ_n^{SOL} is closely related to the cross field particle diffusion coefficient $D_\perp^{\mathrm{SOL}}$. In my bachelor thesis [11] and also in monographies [3, 7] the relationship is derived from simple principles. The result is:

$$D_\perp^{\mathrm{SOL}} = \frac{c_s \lambda_n^2}{2L}. \tag{2.3}$$

where c_s is the sound speed and L is the connection length, i.e. the distance from one target to the other. The sound speed in a plasma is given by the formula:

$$c_s = \sqrt{\frac{kT_i + ZkT_e}{m_i}}. \tag{2.4}$$

The cross field diffusion coefficient in a magnetized plasma derived by classical theory[1] in [25] is given by the formula (for temperature isotropy $T_\parallel = T_\perp = T$):

$$D_\perp^{\mathrm{SOL}} = \frac{kT}{m\nu}\left(\frac{1}{1 + (\omega_c/\nu)^2}\right) \propto \frac{1}{B^2} \tag{2.5}$$

where ω_c is the cyclotron frequency and ν is the plasma collision frequency[2]. It is important to note that this diffusion coefficient is inversily proportional to the square of the magnetic field. It was experimentally found that measured SOL lengths are much higher than the ones predicted by the classical formula 2.5, [7]. This neo-classical transport is caused by drifts arising from the inhomogenity and curvature of the magnetic field. An attempt has been made to take drifts into account by Bohm, resulting in a formula where $D_\perp^{\mathrm{SOL}} \propto \frac{1}{B}$. However, this one still underestimates the diffusion coefficient and thus λ_n^{SOL}. This suggests that cross field transport in the SOL is governed by turbulent processes which are not fully understood. Consequently, empirical scalings must be used to determine λ_n^{SOL} for future machines.

2.3.2 Description of the two point model

This is the simplest model of the divertor SOL, only relating target quantities (T_{t}, n_{t} etc.) to upstream quantities (T_{u}, n_{u} etc.), assuming the following:

1. **Particle balance** Neutrals recycling from the targets are all ionized in a thin layer immediately in front of the target. Furthermore, a neutral which was

[1] In this case, by classical theory, kinetic treatment is meant, with the derivation of the diffusion coefficient done using first order perturbation theory

[2] The collision frequency will be defined in section 4.5

produced by an ion impacting the target while traveling on a specific magnetic field line is assumed to be re-ionized on the same field line. Thus, the only non-zero parallel plasma flow is in a very thin layer between the ionization point and the target.

2. **Pressure balance** No friction between the plasma flow in the ionization region and no viscosity effects are assumed. Hence, in the entire length of each flux tube $p + nmv^2$ =const.

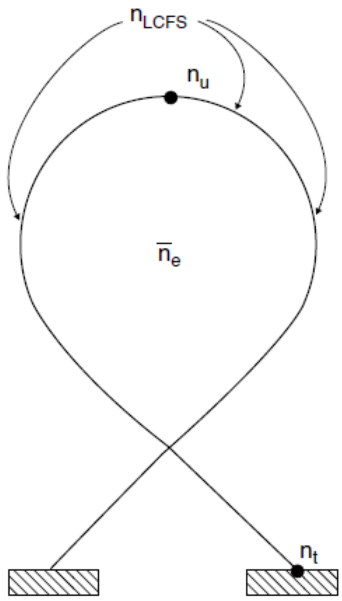

Figure 2.5: Relating the upstream density n_u of two point model to the n_{LCFS} of the 1D radial analysis.

The resulting equations that relate upstream and target parameters are derived in [7]. The equations can be written:

$$2n_{\mathrm{t}}T_{\mathrm{t}} = n_{\mathrm{u}}T_{\mathrm{u}}, \tag{2.6}$$

$$T_{\mathrm{u}}^{7/2} = T_{\mathrm{t}}^{7/2} + \frac{7}{2}q_{\|}\frac{L}{\kappa_{0e}}, \tag{2.7}$$

$$q_{\|} = q_{\mathrm{t}} = \gamma n_{\mathrm{t}} k T_{\mathrm{t}} c_s, \tag{2.8}$$

where $q_{\|} = q_{\mathrm{t}}$ is the heat flux density entering the sheath, γ is the sheath heat transmission coefficient, $\gamma \simeq 7$. Next, the electron parallel conductivity coefficient κ_{0e} is used, assuming electrons and ions are thermally coupled, and neglecting parallel ion heat conductivity as comparatively small, see [7].

Equations 2.6, 2.7, 2.8 are three equations for three unknowns. The unkown parameters are n_t, T_t, T_u while n_u and $q_{\|}$ are regarded as control parameters. n_u reflects the value of the line averaged density, $\langle n_e \rangle_{\text{lav}}$, which in principle is an externally controllable quantity. By taking the crudest case which assumes that:

- The walls are completely hydrogen-saturated from the beginning of the discharge.
- No hydrogen-releasing surfaces are present.
- No pumping is present.

Under these assumptions the line averaged desnity $\langle n_e \rangle_{\text{lav}}$ in the vessel would be given by the amount of gas atoms used to fill the vessel. $\langle n_e \rangle_{\text{lav}}$ is a quantity that is routinely measured on tokamaks and is used for feedback control of the plasma density. Therefore from now on it will be considered a controlable parameter. Next, assuming all ionization occurs in the SOL and assuming only diffusive radial transport in the main plasma, then, the line averaged density is equal to the separatrix density, $\langle n_e \rangle_{\text{lav}} = n_{e,\text{sep}}$.

The next question is what is the relationship between $n_{e,\text{sep}}$ and the n_{u} from the two point model. Assuming a constant upstream density, which is reasonable for a conduction-dominated SOL, where T_e is also constant and using the pressure balance equation one gets that n_u is also approximately constant, except for the region close to the targets. This implies that a the most simple relation can be assumed: $n_{e,\text{sep}} = n_{\text{u}}$. However this is only valid for field line on the separatrix. By moving radially outboard, one must adjust the density by the exponential factor given by equation 2.2.

As for $q_{\|}$, the closest engineering parameter that it can relate to is the input power, P_{in}. In a case where fusion power is negligible, one can write the following:

$$P_{\text{SOL}} = P_{\text{in}} - P_{\text{main,RAD}}, \tag{2.9}$$

where P_{SOL} is the power crossing the separatrix and $P_{\text{main,RAD}}$ is the power radiated from the main plasma. To know the radial $q_{\|}$ profile, one must know the characteristic power width in the SOL. This is derived in [7], section 5.7. For now it will be assumed that $q_{\|}$ can be externally regulated.

2.3.3 Important results from the two-point model

One of the most imporant result we get from the two point model is the equation for the target temperature. By combining equations 2.6 and 2.8 we obtain

$$T_{\text{t}} = \frac{m_i}{2e} \left(\frac{2q_{\|}}{\gamma e n_u T_u} \right)^2. \tag{2.10}$$

This equation still contains the unkown T_u so it is not usable but by doing additional treatment the following equation can be derived:

$$T_{\text{t}} = \frac{m_i}{2e} \left(\frac{2q_{\|}}{\gamma e n_u} \right)^2 \left(\frac{7}{2} \frac{q_{\|} L}{\kappa_{0e}} \right)^{-4/7}. \tag{2.11}$$

This expression holds for the case where parallel heat transport is conductive. Since we want T_t as low as possible, it is positive that $T_\mathrm{t} \propto \frac{1}{n_\mathrm{u}^2}$. Hence the most direct way to drive down divertor temperature is to increase $\langle n_e \rangle_\mathrm{lav}$. Fortunately, a higher $\langle n_e \rangle_\mathrm{lav}$ leads to a higher fusion power which is needed to fulfill the Lawson criterion.

2.3.4 Regimes of divertor operation

In this section, various modes of divertor operation will be briefly introduced.

The sheath limited regime (SL)

In this regime, all the ionization happens in the main plasma. The temperature in the SOL is constant in the parallel direction, $\nabla_\parallel T = 0$. Only the plasma sheaths acts as a plasma sink, thus all the power crossing the separatrix impinges on the solid surface. Typically, this surface can be very small, leading to substantial damage of the divertor targets (or limiters). Therefore, this regime is absolutely inappropriate in a reactor. Moreover, it is more typically observed on limiter configurations. For divertors, this case is typical for low main plasma densities (which is in accord with the two-point model). The temperature at the targets is typically higher compared to the other regimes.

The conduction limited regime/High recycling regime (HRR)

Here, ionization does already appear in the SOL. The power flux from the main plasma ionizes neutrals in front of the target. This ionization cools the target plasma down substantially, and thus $\nabla_\parallel T \neq 0$. The temperature gradient drives power being transported via conduction. The constant pressure in the flux tube cause that also $\nabla_\parallel n \neq 0$. The main particle source is the first wall and the power source is the plasma. This beneficial effect can be amplified by longer connection length. Typically, this regime can be easily recognized by peaking density at the divertor targets. A suitable diagnostic for this are divertor Langmuir probes which measure the ion saturation current, I_sat, which is proportional to the local density. Langmuir probe operation will be described in the next chapter.

Detached regime

The gas density in front of the target prevents the plasma ions to reach the target, causing the plasma density at the target to decrease. A dense cloud of neutral particles forms adjacent to the target. The power is transferred exclusively by conduction and radiation, which causes the power to be more evenly distributed to the targets, since radiation causes volumetric power loss. There is gradually no contact between plasma and the solid (full detachment).

High neutral density in front of the target is also beneficial for the pumping. Next, detachment allows for high separatrix temperatures and the plasma is better screened from impurities.This effect can be enforced by impurity seeding into the divertor. In complete detachment it is difficult to control the gas cloud size, and this can cause a MARFE radiative instability. Thus, partial detachment is foreseen for the reactors including ITER.

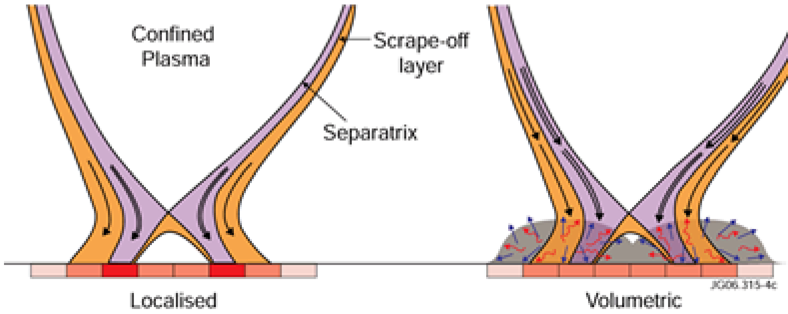

Figure 2.6: Comparsion of a highly localized power loss in the divertor, typical to a sheath limited regime, to a volumetric, more evenly distributed power loss, typical for the HRR and detached regimes.

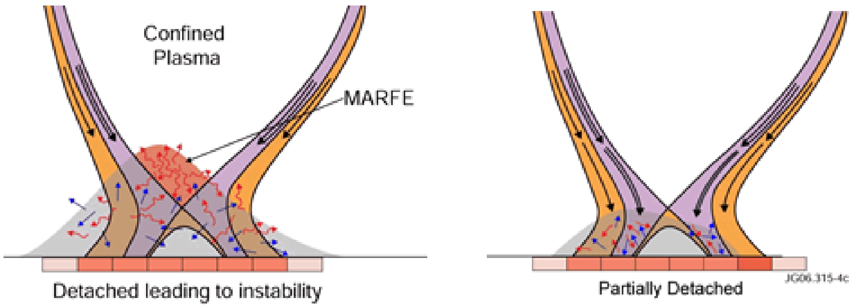

Figure 2.7: Illustration of a fully detached regime leading to a MARFE instabilty (this means that the neutral gas cloud extends beyond the x-point) and a semi detached regime which is a perspective regime for a reactor.

2.4 2-D Fluid modelling of the SOL

Within this thesis, results from 2-D edge codes (e.g. B2, EDGE2D) are used as input for modelling of target EVDFs. A basic outline will be given of how these codes work in this section.

Codes of this type solve the electron and ion fluid equations on a 2-D grid which is separatly calculated and in principle is given by the magnetic flux surfaces. The two coordinates are the radial coordinate and the parallel coordinate (the parallel coordinate can be alternatively projected into the poloidal plane to become the poloidal coordinate). A typical grid can be seen in Fig. 2.8

The electron and ion fluid equation comprise the equation for particle, momentum and energy balance (to see their exact form, see [7], p. 450). The equation also contain particle, momentum and heat sources/sink terms arising from neutrals. The calculation of these terms requires the use of a coupled hydrogen neutral code such as DEGAS, EIRENE, NIMBUS, etc. These require as input the spatial distribution of n_e, T_e and T_i, and the code then outputs the source/sink terms due to the plasma–neutral interactions. The plasma model and the neutral model must thus be solved iteratively [7].

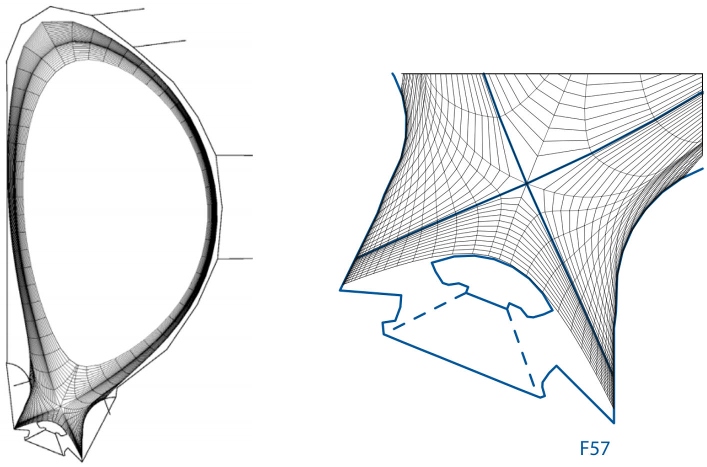

(a) (b)

Figure 2.8: An example of a typical 2-D grid from the B2 code (SOLPS) for ITER. (a) depicts the whole grid, (b) is the divertor close-up.

As for boundary conditions, for this 2-D case, according to [7] we have 4 distinct boundaries:

(a) The LFCS: a specified density n_e mid-way between targets on the LCFS, or inner flux surface used as the boundary and the total heat inflow in the electron and ion channels.

(b) The two targets. Here, the boundary conditions are not straightforward to define and are related to numerics. Details can be found in [7], p. 434.

(c) The wall side: Various boundary conditions are used, for example: $n_w = T_{ew} = T_{iw} = 0$

2.5 The JET divertor

After the brief overview of basic divertor physics given in the previous chapters, let us have a look at a specific divertor. Since this thesis deals with JET it is natural that a basic description of the JET divertor will be given.

The present JET divertor has been installed during the 2011 shutdown in the frame of the ITER-like wall project. The aim of this project is to test the properties of wall materials chosen for ITER in tokamak conditions. Briefly, the ITER like wall comprises of:

- Beryllium (Be) PFCs in the main chamber.
- Tungsten (W) divertor target plates.

Tungsten is used at the high heat flux surfaces due to its ability to withstand extremely high temperatures, with a melting point of 3442 °C. On the other hand, with an atomic number of 74, it causes substantial cooling of the plasma when going through all its ionization states after being sputtered out from the wall.

In contrary, Beryllium has an atomic number of 4. Of course it can only be used at locations where heat fluxes are low, like the main chamber wall, since it melts at 1287 °C.

As for the geometry, it succeeds the previous CFC divertor which was installed during the 2004/2005 shutdown and was designated to accommodate ITER-relevant high triangularity plasmas (up to $\Delta = 0.5$) while keeping operational flexibility for other scenarios [9].

The divertor is shaped to optimize the wetting fraction without exposing sharp edges to high power loads. This is done by tilting of divertor target plate tiles with respect to the field line inclination in a way that the leading edge of the next tile is fully shaded.

Poloidal cross-sections of the old CFC divertor and the new ITER-like divertor are in Fig. 2.9.

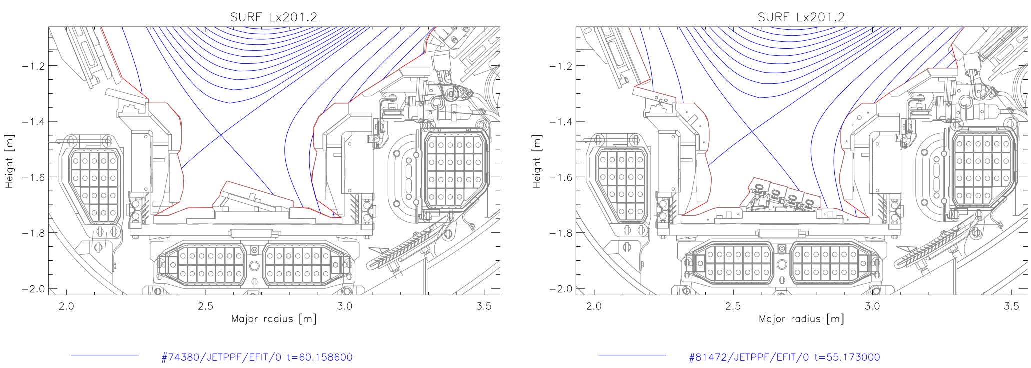

(a) (b)

Figure 2.9: Poloidal cross sections of the JET CFC divertor (a) and the ITER-like tungsten divertor (b) and of the poloidal field coils used to generate the magnetic field needed to create the x-point. It can be seen that the divertor geometry is the same. A notable difference can be seen at the outer horizontal target for the W divertor (b), where the target plate is form of four actively cooled full W monoblocks. The rest of the target areas of (b) are W-coated.

Chapter 3

Electrical probes in tokamaks

3.1 Introduction

There is a large variety of types of electrical probes used in tokamaks and in most cases they are relatively simple and inexpensive devices. The most simple electrical probe is the single Langmuir probe, which is literally a piece of wire in the plasma. These probes have been the work horse of edge plasma research since the early days of tokamak research. However, the simplicity of the construction is redeemed by the complexity of the interpretation. They can be inserted into limiters or divertor targets in large arrays or into reciprocating drive mechanisms for probing deeper in the SOL. In the first case, the Langmuir probes are non-disturbing for the plasma, in the second case they behave as a perturbative diagnostic.

Other probe types evolved from the simple Langmuir probe and can be combination of several single probes, or have some structure around them which shields them from some types of particles etc. Each probe type has its benefits but also drawbacks. Basic single Langmuir probe theory will be given in this chapter as well as an overview of several other frequently used probe types.

3.2 The Single Langmuir probe

The single probe (SP) is virtually a conductive wire facing the plasma and is typically built into the limiter or divertor target plate. The basics of the theory are listed in this section, as well as some aspects of data analysis of real experimental data from SPs.

3.2.1 Basic SP theory

The theory of the SP is based on the theory of the plasma sheath. Electrons have a much larger mobility than ions (in other words, an electron with the same energy as an ion has much higher velocity) and are quickly attached to any electrically insulated conductive object inserted into the plasma, charging it to a negative potential. Since the probe is insulated, the potential adjusts in a way that the total current flowing to the probe is zero, $j_{\rm prb} = 0$. This potential is called the floating potential, $V_{\rm fl}$. For the total current, we can write:

$$j_i + j_e = 0 \tag{3.1}$$

This is de facto the ambipolar condition written in terms of current densitites instead of flux densities. The ion current is given by the Bohm sheath criterion, [7]:

$$j_{\rm i} = en_{\rm se}c_{\rm s}, \tag{3.2}$$

where $n_{\rm se}$ is the density at the sheath edge ($n_{\rm se} = n_{\rm i,se} = n_{\rm e,se}$) and c_s is the sound speed, see 2.4.

As for the electron current density, this can be simply calculated. Let the electron temperature at the sheath edge be T_e. The electron flux entering the sheath is given by the Maxwellian distribution. However, not all electrons can overcome the repulsive sheath. Since the plasma potential is considered to be 0, the potential drop in the sheath is equal to the floating potential $V_{\rm fl}$. Only energetic electrons, with energies larger than $-eV_{\rm fl}$ (the floating potential is negative) are collected by the probe surface. This defines a cutoff energy and velocity, $E_{\rm cut} = -eV_{\rm fl}$ and $v_{\rm cut} = \sqrt{-2eV_{\rm fl}/m_e}$, respectively. Let us calculate the electron current denstiy to the probe by integrating a the Maxwellian VDF in the correct limits:

$$j_{\rm e} = -en_{\rm se}\int_{v_{\rm cut}}^{\infty} v f(v){\rm d}v, \tag{3.3}$$

where $f(v)$ is a 1-D Maxwellian velocity distribution:

$$f(v) = \left(\frac{m_e}{2\pi kT_e}\right)^{1/2} \exp\left(-\frac{m_e v^2}{2kT_e}\right). \tag{3.4}$$

After evaluating the integral 3.3 we get for the electron current density:

$$j_{\rm e} = -en_{\rm se}\sqrt{\frac{kT_e}{2\pi m}} \exp\left(\frac{eV_{\rm fl}}{kT_e}\right). \tag{3.5}$$

Now, using equations 3.5 and 3.2 in 3.1 the floating potential can be expressed:

$$V_{\rm fl} = \frac{1}{2}\frac{kT_e}{e}\ln\left(2\pi\frac{m_e}{m_i}\left(1 + \frac{T_i}{T_e}\right)\right). \tag{3.6}$$

First, one can note that the floating potential has no dependence on density, $n_{\rm se}$ has canceled out. Second, from the formula one can see that $V_{\rm fl} < 0$. One may also note that for hydrogenic plasmas, $eV_{\rm fl}/kT_e \approx 3$.

Let us recall that in this case, the electron and ion flux densities are equal at the probe surface, $j_i = -j_e$. Next, let us consider a probe that is not floating, but that is connected the plasma via an external circuit. A potential difference can be applied via an external power supply, see Fig. 3.1. In this case, net current is drawn through the circuit, hence at the probe surface, $j_i \neq -j_e$. The return surface is typically the divertor target surface or limiter surface.

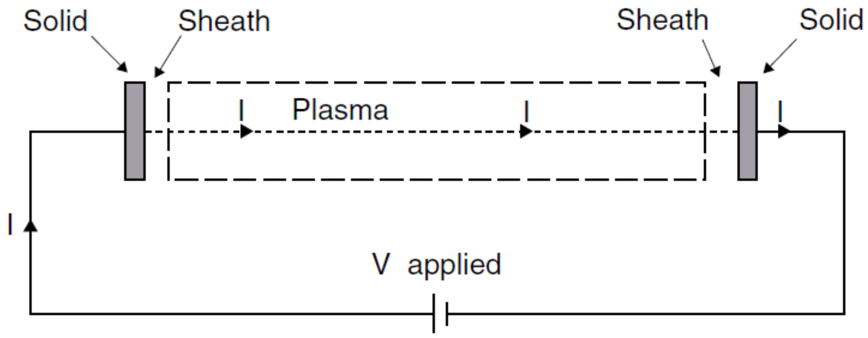

Figure 3.1: The probe circuit with an external power supply. One of the solid surfaces can be considered the probe surface and the other is the return surface. There is either no magnetic field, or **B** lies along the current direction [7]

Now let us consider the case when we apply a biasing voltage V to the probe and close the circuit by returning the current to the plasma. The net current density j_{prb} to a probe biased to a potential V can be expressed:

$$j_{\text{prb}} = en_{se}c_s\left(1 - \exp\left(\frac{e(V - V_{fl})}{kT_e}\right)\right), \tag{3.7}$$

The derivation is similar to the derivation of the floating potential. It is important to note that

$$\lim_{V\to-\infty} j_{\text{prb}}(V) = en_{\text{se}}c_s. \tag{3.8}$$

Thus when the probe is biased sufficiently negatively, all the electrons are repelled and all that remains is the ion current. This current is called the *ion saturation current* and is given by the equation

$$j^+_{sat} = en_{se}c_s. \tag{3.9}$$

3.2.2 3-parameter fit

Next, it will be shown how single probe experimental characteristics are treated using the *3-parameter fit*, the most ordinary treatment[1], in order to yield the quantities of interest, namely the electron temperature T_e and density n_e at the probe. Let A_{prb} be the area of the probe and let the magnetic field **B** be parallel to the normal vector of the probe surface. Then the total current passing through the probe is

$$I_{prb} = j_{prb}A_{prb}. \tag{3.10}$$

[1]This treatment is the one most frequently used and is sometimes refered to as the "classical" treatment [27].

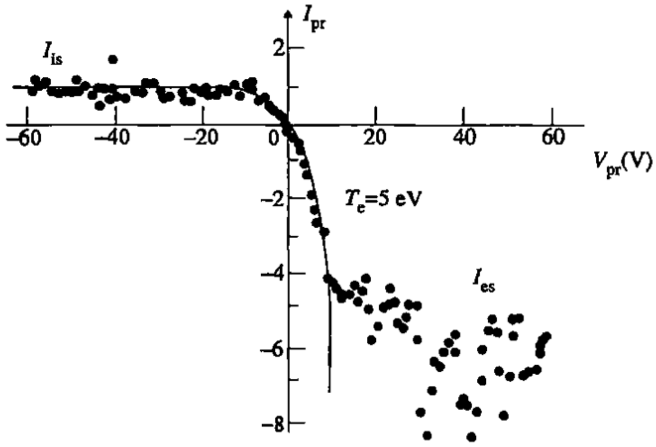

Figure 3.2: A SP IV characteristic from the T-10 tokamak with low ion to electron saturation current ratio. Here, the reference potential is set to be equal to the floating potential, $V_{\mathrm{fl}} = 0$ [3]

Combining equations 3.7, 3.9 and 3.10 gives the theoretical IV characteristic of the probe

$$V_{prb} = \frac{kT_e}{e} \ln \left(1 - \frac{I_{prb}}{I^+_{sat}} \right). \tag{3.11}$$

Consequently, a logarithmic fit of V_{prb} against I_{prb} yields a measurement of T_e. Or, even more frequently, this is done the other way around, fitting I_{prb} as a function of V_{prb} using an exponential fit according to 3.15. It is very important to note that equations 3.11 and 3.15 hold only for probe potential which are lower than the plasma potential. If the probe potential equals the plasma potential, no sheath electric field is present and electrons are not repelled by the sheath anymore, flowing to the probe at a thermal velocity distribution. If the probe is biased sufficiently positively, all that remains is the electron current. This is called electron saturation, and the *electron saturation current* is given by

$$I^-_{sat} = -\frac{1}{4} e n_{\mathrm{se}} \langle v_e \rangle, \tag{3.12}$$

where $\langle v_e \rangle$ is the electron thermal speed and n is the electron density just at the probe. Since electrons carry the same absolute charge but are much lighter, electron saturation current is greater than the ion saturation current by the ratio $(m_i/m_e)^{1/2} \approx 60$ for a hydrogen plasma. This seems to work as far as the plasma is not magnetized. In tokamaks, however, for values of V_{prb} causing electron saturation, electron to ion saturation current ratios are much smaller. Fig. 3.2 shows a typical SP IV characteristic in the T-10 tokamak. The electron part of the probe characteristic is usually not used, only the ion part is fitted. The fitting equation, the same as 3.7

but written in terms of total currents instead of current density, can be written:

$$\boxed{I_{\text{prb}} = I^{+}_{\text{sat}}\left(1 - \exp\left(\frac{e(V - V_{fl})}{kT_e}\right)\right).} \tag{3.13}$$

Hence, the fit yields the 3 unknown parameters: I_{sat}, V_{fl}, T_e. This is why the fit is frequently referred to as the *three-parameter fit*. The plasma potential is often unknown and thus there are several methods up to which voltage real IV characteristics like the one in Fig. 3.2 are fitted in experimental practice. These can be listed, according to [26] as follows:

- **Fitting until the floating potential** $V_{\text{prb}} < V_{\text{fl}}$. Since it is a more complex problem to interpret the electron part, just the ion-dominated part of the IV-characteristic is taken into account by fitting I_{prb} for $V_{\text{prb}} < V_{\text{fl}}$ while $V_{\text{prb}} > V_{\text{fl}}$ is ignored. The drawback of this method is evident. Since for a hydrogen plasma at zero plasma potential, the floating potential of a single probe is $V_{\text{fl}} \approx -3kT_e/e$, from section 3.2.1. **This means that we only take into account the electrons that have a higher energy than $3kT_e$, which only corresponds to a small fraction of electrons from the distribution**. This way, only the energetic tail of a distribution function plays a role in this analysis. Thus a small perturbation in the tail of the distribution may lead to incorrect values of T_e deduced by this method. The assessment of the magnitude of this effect is one of the principal goals of this thesis and is the subject of chapters 4 and 5.

- **Minimizing** T_e. This method also uses the ion part of the disribution but the potential up to which the IV characteristic is fitted is adjusted in a way that T_e from the fit is minimized. Of course the fit is performed at least until V_{fl}. This method arises from experimental practice, since it is frequently reported that probes tend to overestimate the electron temperature compared to other diagnostics (e.g. divertor Thomson scattering, spectroscopy) for some cases, see [20, 21].

- **Minimizing the fitting error** The value of the probe potential $V_{\text{prb}} > V_{\text{fl}}$ is adjusted in a way that the error of the fit is minimal.

Deducing the density

The I_{sat} output parameter from the 3-parameter fit directly gives a measurement of the electron density at the sheath edge:

$$I^{+}_{sat} = A_{prb} e n_{se} c_s. \tag{3.14}$$

However, to calculate c_s we need to know the ion temperature. It is a usual practice to assume $T_e = T_i$ for collisional (i.e. dense and relatively cold) SOL plasmas.

3.2.3 4-parameter fit

In some cases, typically for high recycling and detached divertor conditions (see section 2.3.4) the ion current does not saturate, based on manual inspection of the probe IV characteristics [28]. Instead, it tends to increase linearly with decreasing bias voltage. This behaviour is due to expansion of the electrostatic sheath into the plasma around the probe, and is often observed on tokamak LP characteristics [29]. Fig. 3.3 demonstrates this linear increase for a Tore Supra single probe IV characteristic.

To include sheath expansion, one has to add a term that reflects the linear increase mentioned above to the classical 3-parameter fit 3.15, as proposed in [30]:

$$\boxed{I_{\text{prb}} = I^+_{\text{sat}}\left(1 - \exp\left(\frac{e(V - V_{fl})}{kT_e}\right)\right) + a(V - V_{\text{fl}}),} \tag{3.15}$$

where the coefficient

$$a = \frac{\Delta I}{\Delta V} \tag{3.16}$$

expresses the slope of the linear increase of I_{prb} with decreasing V_{prb} due to sheath expansion. Hence, this fit yields 4 parameters: I_{sat}, V_{fl}, T_e and the slope a. Ignoring sheath expansion can lead to inaccurate fits, as can be seen in Fig. 3.3 and consequently to large errors in the value of T_e measured by the probe.

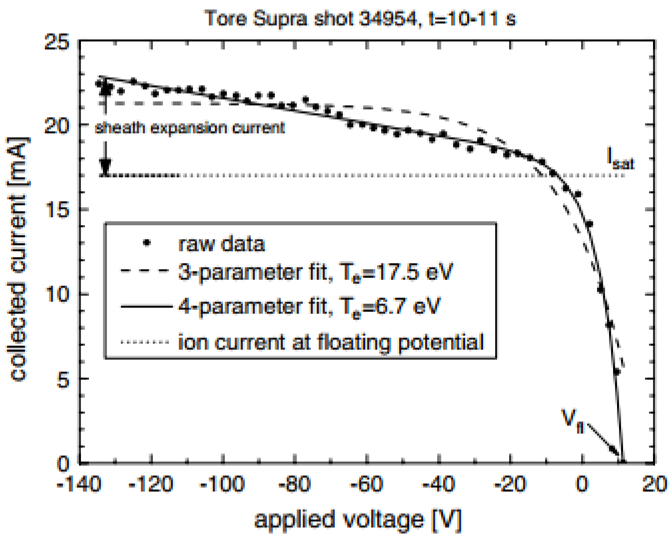

Figure 3.3: IV characteristic from a 5mm diameter dome-shaped single Langmuir probe in the pumping throat of the Tore Supra toroidal limiter. Experimental data are indicated by dots, the best 3-parameter fit by the dashed curve, the best 4-parameter fit by the full curve. The ion current at floating potential calculated by the 4-parameter fit is indicated by the thin dotted line. The increase of ion current above this level for negative voltages is due to sheath expansion. Taken from [29].

3.3 Double probes

A double Langmuir probe is a pair of probe tips close enough to each other so that they are assumed to be exposed to the same plasma conditions. The probes are kept isolated from the torus and are connected across a variable biasing voltage source. Let the currents in each probe tip be I_1, I_2. Taking two identical probes with surface A, defining the power supply voltage $V = V_1 - V_2$, where V_1, V_2 are the respective probe voltages and defining the currents with equation 3.7 the following theoretical relation can be calculated

$$I_1 = I_{sat}^{+} \tanh \frac{V}{2T_e} \tag{3.17}$$

The main advantage of this configuration is that it limits the electron current, preventing destruction of the probe since the electron current typically saturates for much higher absolute values than the ion current.

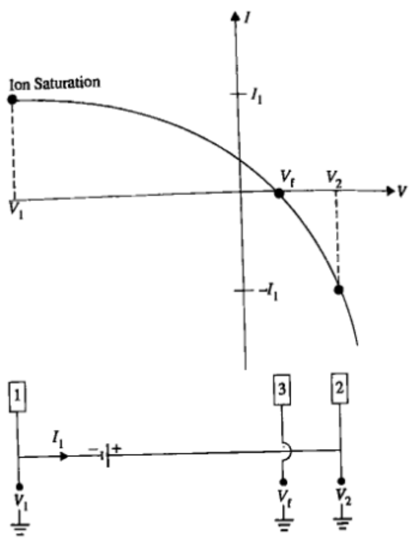

Figure 3.4: Schematic illustration of the triple Langmuir probe configuration. The circuit diagram shows the positions of the probes on the $I(V)$ curve [J. Wesson, Tokamaks]

3.4 Triple probes

Triple Langmuir probes consist of three tips exposed to the same plasma parameters. One of the probe tips measures the floating potential while the other two are coupled and biased with a constant potential so that one tip draws the ion saturation current and the other an electron current, see Fig. 3.4. The potential V_2 on the electron current drawing tip adjusts itself so that the two currents are of the same size. Let

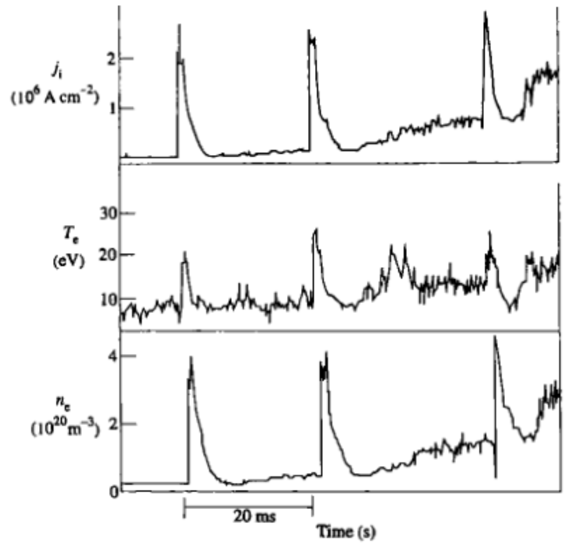

Figure 3.5: Divertor target triple probe measurements during a discharge with ELMs at JET [3].

the tips be identical, of surface A. Again, using equation 3.7 and $I_1 + I_2 = 0$, we get

$$(1 - \exp\left(\frac{e(V_1 - V_{fl})}{kT_e}\right))A + (1 - \exp\left(\frac{e(V_2 - V_{fl})}{kT_e}\right))A = 0. \tag{3.18}$$

Assuming the supply voltage to be large, $kT_e \ll e|V_1 - V_{fl}|$, equation 3.18 gives the following expression for the temperature

$$T_e = \frac{(V_2 - V_f)}{k \ln 2} \tag{3.19}$$

Since in this case V_2, V_{fl} and I_{sat}^+ can be measured at the same time, high time resolution is an advantage of this arrangement (one does not have to sweep through a whole range of probe voltages in contrast to the single probe). Thanks to this triple probes are frequently used to measure discharges with edge-localized modes. Fig. 3.5 shows high time resolution divertor triple probe measurements from JET. However, triple probe data are unreliable in situations when plasma parameters differ across the three probe tips or when I_{sat}^+ and I_{sat}^- are comparable [3].

Chapter 4

Electron velocity distribution model description

4.1 Motivation

Single Langmuir probes are commonly used to measure plasma parameters, such as the electron temperature or plasma density in the plasma edge. The principles of their operation is described in chapter 3.2. It is relatively simple method, however there is a variety of observations showing that under some specific conditions the electron temperature T_e measured by probes can significantly differ from the actual T_e in the SOL. For example, in [20] it is reported that during Ohmic heating in the ASDEX tokamak the T_e measured by Langmuir probes is at least two times higher than the one measured by Thomson scattering. A similar observation is made in [21] at DIII-D. In [13] it is reported that in strongly recombining detached or partially detached divertor plasmas on TCV the expected $T_e \sim 1$ eV is not reproduced by probes. Instead, measured values of approximately $T_e \sim 5$ eV are typical.

Again, from section 3.2 let us recall that due to the fitting of IV characteristics typically up to the floating potential, only the high energy tail of the target electron velocity distribution is taken into account (i.e. only the distribution function for electron energies roughly higher than $3kT_e$ is effectively used for the IV characteristic analysis, which for a Maxwellian is only a few % of the distribution). Since the ion flux to the target is a constant value (neglecting sheath expansion, see 3.2.3), only the electron current plays a role in the form of the IV characteristic and this depends on the exact form of the distribution. For an ideal Maxwellian distribution with temperature T_e, the electron current to the probe would reflect the temperature of this distribution and the fit would yield the correct temperature of the distribution. On the other hand, should the high energy tail of the distribution be represented by a different temperature than the bulk of the distribution (i.e. in the case we had a non-Maxwellian distribution), the electron current and thus also the probe measurement will likely reflect the temperature of this "high energy component". This was confirmed in an analysis by Stangeby [32]. In paper [33], it is found that non-Maxwellian distributions in the CASTOR edge plasma can be represented by *bi-maxwellians*, with one dominant, low temperature bulk electron population and one minority composed of hotter electrons.

Even small perturbations in the "high energy tail" of the distribution, seeming negligible when compared to the bulk of distribution function can lead to an incorrect T_e deduced by the standard IV characteristic fitting method, as we will see. It is important to note that classical probe theory assumes a Maxwellian electron distribution.

Next, it is obvious to ask ourselves whether the EVDF at the divertor target plates is Maxwellian or not. Wesson proposes in [31] that steep parallel temperature gradients in the SOL can be a source of de-Maxwelization of the target EVDF via energetic electrons from the upstream plasma which can travel without collisions to the divertor targets. A numerical approach is proposed in [15] to calculate the effect of hot collisionless upstream electrons on the target EVDF. This approach is adopted in paper [13] to calculate target EVDFs and to deduce synthetic probe measurements from these EVDFs for the TCV tokamak. The same approach, with some refinements is used to calculate target EVDFs for the JET tokamak in this thesis. I will refer the this approach as the *Simple EVDF model* throughout this thesis.

Additionally, de-Maxwellization of the EVDF is also affected by a number of processes in the SOL like inelastic collisions of electrons with neutrals and impurities or fast-time processes like edge-localized modes (ELMs) and blobs [14]. In [14] the electron velocity distribution functions at the targets are computed by an extensive, self-consistent, massively parallel PIC code for a 1-D SOL named BIT1 (this code is capable of computing an immense number of other quantities too). Benchmarking of the simple EVDF model against BIT1 is also one of the goals of this thesis and will be shown in section 5.5.

4.2 Input data

It was stated that the reason for enhancement of the target EVDF tail is believed to be hot upstream electrons when significant T_e gradients are present. Thus in the simple model, 1-D movement of electrons parallel to the field lines will be considered. Therefore, as an input, the model requires parallel $T_e(x)$ and $n_e(x)$ SOL profiles, where x is the connection distance from one divertor target plate at $x = 0$ to the other target plate at $x = L$. The model also includes potential variation. The potential parallel profile $\phi(x)$ canbe estimated by a simplified approach from the temperature profile. Since hte T_e and n_e parallel profiles are practically impossible to measure with sufficient spacial resolution, we must take them from fluid codes, in the case of JET, the EDGE2D-EIRENE code. EDGE2D is a solver for the 2-D plasma fluid equations and is coupled to EIRENE which accounts for interactions with neutrals. The basic principles of this type of plasma simulations is described in section 2.4. The parallel T_e and n_e profiles are one of the many outputs of any converged run of EDGE2D-EIRENE and will be described in the next section.

4.2.1 T_e and n_e profiles

In this section it will be shown how the actual profiles look like and the governing physics behind them will be outlined. The profiles are an output of EDGE2D-EIRENE simulations (with drifts not taken into account) of JET Ex-3.1.2. The objective of this experiment was to perform a low-δ L-mode density scan at fixed input power in order to characterize detached plasmas for the ILW for benchmarking of the EDGE2D-EIRENE code. The corresponing discharges to this experiment are JPNs 81469-81484.

The parallel profiles are shown in subsequent figures 4.1 (n_e) and 4.2 (T_e) for the flux surface situated 5 mm from the separatrix (mapped to the outer midplane). The "guiding parameter" of all the profiles is the midplane density, which is in fact the same as the upstream density, due to the typical plateau in the middle of the density profiles (i.e. these terms are equivalent).

EDGE2D-EIRENE simulations are steady state simulations (time independent), each of these profiles is part of the solution of one entire converged EDGE2D-EIRENE run for a given set of (experimentally measured) input parameters. Hence the obtained profiles can be regarded as the actual profiles at the time when the input parameters were measured. This is important when one needs to compare EDGE2D-EIRENE prediction with other diagnostics. Naturally this holds for the simple EVDF model too, since it uses these EDGE2D-EIRENE profiles as input. This will become important once we will need to compare the results of the simple model to experimental single probe measurements. For now, the time is represented by the value of the upstream density, which increases from 3.3×10^{18} m^{-3} to 21.1×10^{18} m^{-3} throughout the density ramp.

After a closer look at the shape of the parallel T_e, n_e profiles, one can distinguish between three distinct types of profiles, roughly corresponding to divertor operating regimes:

(a) **Low density case (Sheath limited regime)**

This group is represented by upstream densities 3.3, 4.5, 7.5×10^{18} m^{-3}. Here, T_e and n_e in Fig. 4.2 and 4.1 are more or less constant, indicating a sheath-limited/low recycling regime, whith most of the ionization happening oustide the SOL, i.e. in the main plasma. The divertor targets act as plasma sinks, which can be seen in the decrease of n_e at both targets.

(b) **Medium density case (High recycling regime)**

Upstream densities: 9.7, 11.1, 12.2, 14×10^{18} m^{-3}. Here, due to higher SOL density, ionization is localized at the targets. This cools the target plasma, bringing the target T_e down, Fig. 4.2, thus forming a significant temperature gradient. n_e increases substantially at the divertor targets, Fig. 4.1. These profiles represent high recycling regimes.

(c) **High density case (Partially detached regime)**

Upstream densities: 16.2, 17.7, , 21.1×10^{18} m^{-3}. Here, the density is so high that the plasma begins to detach from the targets. The target densities, Fig. 4.3 start

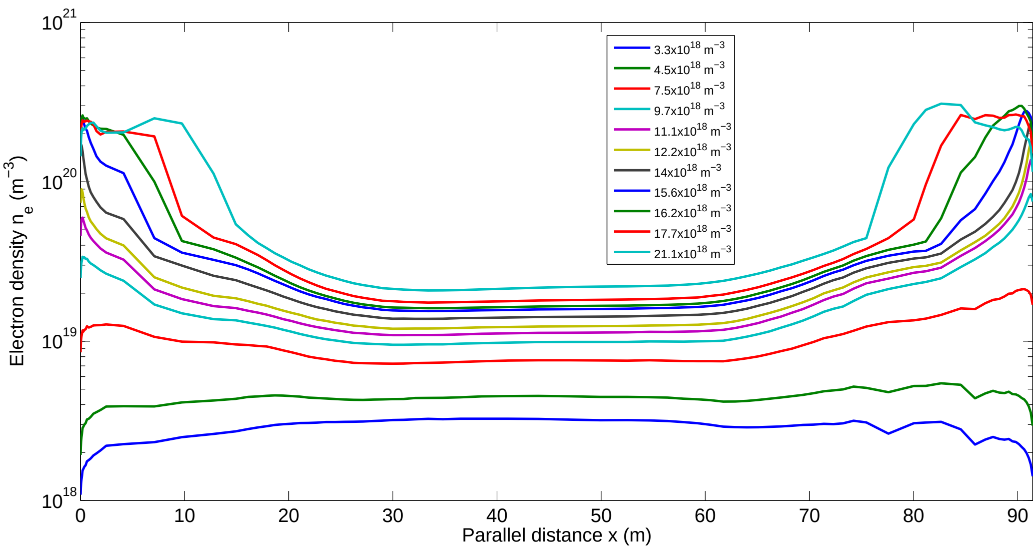

Figure 4.1: Parallel n_e profiles generated by EDGE2D-EIRENE for the flux surface situated 5 mm from the separatrix for JPN 81469. A total of 11 profiles each corresponding to an upstream density, being ramped up from 3.3×10^{18} m^{-3} to 21.1×10^{18} m^{-3}. For low upstream density n_u cases, the density profile is flat, with increasing density we enter the high recycling regime (n_e peaking at the divertor targets) and for the highest upstream densities the targets start to detach, i.e. n_e at the targets starts to decrease.

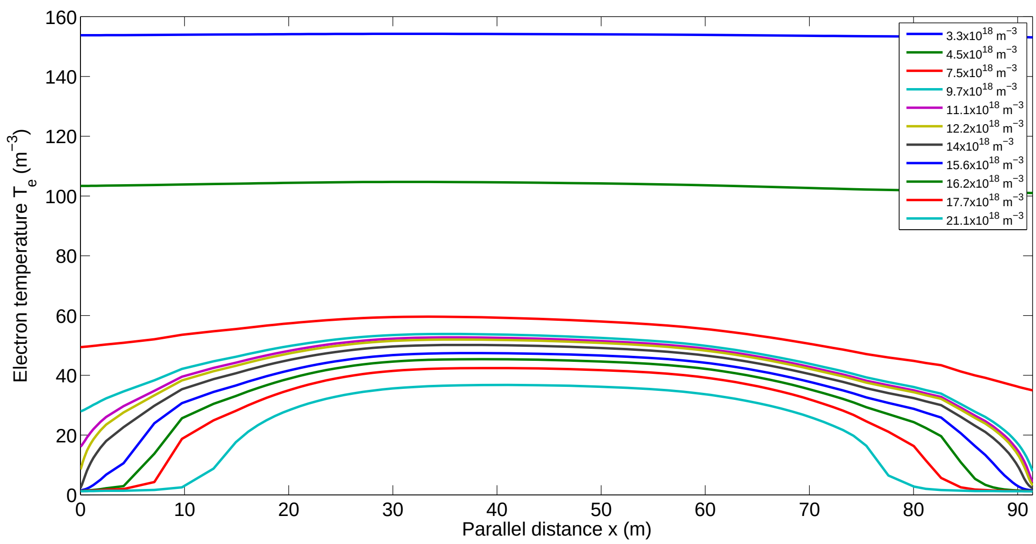

Figure 4.2: Parallel T_e profiles generated by EDGE2D-EIRENE for the flux surface situated 5 mm from the separatrix for JPN 81469. A total of 11 profiles each corresponding to an upstream density, being ramped up from 3.3×10^{18} m^{-3} to 21.1×10^{18} m^{-3}. One may note the decreasing temperature at the targets for increasing upstream density, in accordance with the two-point model described in section 2.3.3.

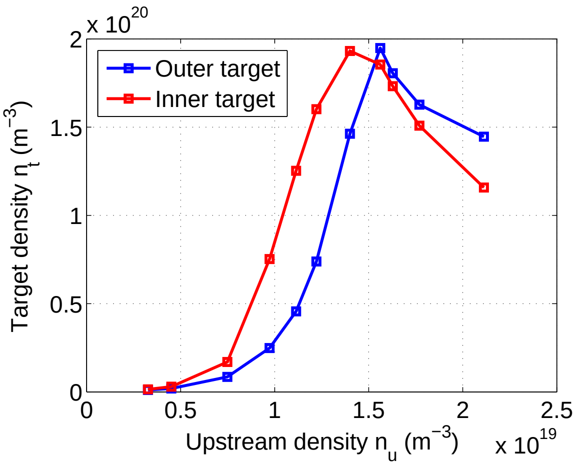

Figure 4.3: Divertor densities as a function of the upstream density from the EDGE2D-EIRENE code, simulating the density ramp discharge JPN 81469. The upstream density is increased from 3.3×10^{18} m^{-3} to 21.1×10^{18} m^{-3}. The target density n_t increases until the density rollover at 15.6×10^{18} m^{-3} (Outer target) and 14×10^{18} m^{-3} (Inner target) due to beginning detachment of the targets.

to decrease, while the density peaks, which represent the ionization front, move further upstream, 4.1. This upstream movement of the ionization front can be well identified on the temperature profiles as well, Fig. 4.2.

4.2.2 Potential ϕ parallel profile

As it was mentioned, the simple model accounts for potential variation. The potential can be calculated from the temperature profile, as suggested in [15]. This is a consequence of Ohm's law in a 1-D SOL plasma, derived from the 1-D momentum equation, from [7] p. 392:

$$\frac{ej_\parallel}{\sigma_\parallel} = -e\frac{\mathrm{d}\phi}{\mathrm{d}x} + 0.71\frac{\mathrm{d}kT_e}{\mathrm{d}x} + \frac{1}{n_e}\frac{\mathrm{d}p_e}{\mathrm{d}x} \tag{4.1}$$

Where $j_\parallel$ is the parallel electric current, $\sigma_\parallel$ is the electric conductivity, p_e the electron pressure, x the parallel coordinate. Since p_e is constant, and no parallel currents are assumed to exist, or other complications, for the potential we have:

$$\phi(s) = 0.71k/e(T_e(x) - T_e(0)) \tag{4.2}$$

Hence, the electrons are attracted in the direction of the temperature gradient.

4.3 Computation of the target EVDF

Fast electrons from the warmer upstream regions can under certain conditions travel collisionlessly to the targets, thus affecting the local distribution function there. The contribution of these electrons to the target EVDF is constructed numerically. The

$T(x), n(x), \phi(x)$ profiles are assumed to be specified. Next, the method to compute the target EVDF will be described. It is similar to the one described in my bachelors thesis [11] with some refinements which will be pointed out by footnotes:

1. First, a specific value of v is chosen at the target. The parallel x-coordinate at the target is, naturally, $x = 0$.

2. Next, the mean free path $\lambda(n_e, T_e, v)$ of the electron with velocity $v(0)$ in the target plasma characterised by $T_e(0)$ and $n_e(0)$ is calculated. The choice of the formula for the mean free path is an important player in the analysis and will be discussed in section 4.5. Although the exact value of the mean free path does not affect the form of the EVDF construction, it can affect the actual numerical results.

3. Now, a small step, typically a small fraction of the local mean free path Δx upstream is taken. The x-coordinate of the electron is now $x = 0 + \Delta x$.

4. Subsequently, the probabilty of a collision occuring during this step is calculated classicaly, $\mathrm{d}p = \frac{\Delta x}{\lambda}$.

5. During the step, in consequence of the potential change, the velocity changes too. The new velocity is found, from energy conservation (for an arbitrary position in the parallel direction x):

$$v(x) = \sqrt{v_0^2 + \frac{2e}{m_e}(\phi(x) - \phi(0))} \tag{4.3}$$

6. Again, the mean free path $\lambda(v(x), T_e(x), n_e(x))$ and the probability of collision during the next step $\mathrm{d}p(x)$ is computed.

7. The procedure described above is repeated. As the electron advances further and further upstream, the total probability of collision accumulates. The accumulated probability of collision at an arbitrary point x upstream is the sum of the probabilities of collision during each step and is a function of the distance from the target x. The accumulated probability can be written as

$$p(x) = \int_0^x \mathrm{d}p(x') = \int_0^x \frac{\mathrm{d}x'}{\lambda(v(x'), x')} = \int_0^x \frac{\mathrm{d}x'}{\lambda(v(\phi(x'), v), T_e(x'), n_e(x'))}. \tag{4.4}$$

8. It is assumed that a Maxwellian EVDF exists $f^{\mathrm{Max}}(v)$ at every point x along the field line. The target electron velocity distribution function is then evaluated as a "weighted average" of EVDFs along the field line from $x = 0$ until $x = L$:

$$f(v_0) = \frac{\int_0^L S(x) f^{\mathrm{Max}}(T_e(x), n_e(x), v(x))\mathrm{d}x}{\int_0^L S(x)\mathrm{d}x}, \tag{4.5}$$

where the weighting function $S(x) = \exp(-p(x))$ represents a suitable electron source distribution [13]. The physical meaning of this weighting function is that electrons originating closer to the target have a greater chance of reaching the target than from sources further upstream, thus EVDFs closer to the target count more in integral 4.5.

9. By repeating this process for a range of initial values $v(0)$, the entire EVDF at the target is constructed.

At this point it is important to point out that the method described above has two improvements compared to the model used in the bachelor thesis [11].

First, the step length Δx was originally constant. This was found to cause problems in the calculation, for values of the mean free path that were smaller than the step length. This was solved by introducing an adaptive step length defined as a small fraction of the local mean free path.

Second, the EVDFs were averaged only up to a certain point defined by the "last collision", the point where the cumulative probability function $p(x)$ reached unity. In the diploma thesis, however, the EVDFs are averaged along the whole collision length. The smaller probabilty of an electron arriving from far upstream is expressed by the weighting function $S(x) = \exp(-p(x))$.

4.4 Computing the target probe IV characteristic

Now that the synthetic EVDF simulating the "real" EVDF at the target is known, the divertor target probe synthetic IV characteristic can be computed. The calculations are based on theory described in chapter 3. This is done by calculating the *cutoff velocity* v_{cutoff}, the minimum velocity at which electrons can overcome the sheath potential of an electrically floating probe, section 3. For a floating probe, the ambipolar condition must be satisfied:

$$j_{prb}^{-} = j_{prb}^{+}. \tag{4.6}$$

By substituting the equations for ion and electron currents, 3.2 and 3.3, respectively, the following equation is obtained (it is important to note that here $f(v)$ is our computed synthetic EVDF, not necessarily a Maxwellian):

$$\int_{v_{\text{cutoff}}}^{\infty} v f(v) \mathrm{d}v = \sqrt{\frac{2kT_e(0)}{m_i}}. \tag{4.7}$$

The only unknown parameter in this equation is the cutoff velocity v_{cutoff} and so it can be determined from this equation. In the code, this is done by an iterative method. Once this has been done, the actual IV characteristic can be constructed. We can not do this by simply using the equation 3.15, since our computed distribution is not necessarily a Maxwellian.

Now, a potential V_{prb} shall be applied to the probe. This potential defines a new velocity w at which electrons can overcome the sheath. Since a floating probe is biased negatively, an applied potential will decrease the velocity necessary to overcome the total potential, thus giving w as

$$w = \sqrt{\frac{2}{m_e}\left(\frac{1}{2}m_e v_{\text{cutoff}}^2 - eV_{prb}\right)}. \tag{4.8}$$

The new electron current to the probe is given by

$$j_{prb}^{-}(V_{prb}) = e\int_{w}^{\infty} v f(v)\mathrm{d}v. \tag{4.9}$$

The ion current remains unchanged and so net current is now drawn through the probe. This current is easily given by subtracting the electron current from the ion current,

$$j_{prb}(V_{prb}) = j_{prb}^{+} - j_{prb}^{-}(V_{prb}). \tag{4.10}$$

It is important to note that this calculation is done in a way that if $V_{\text{prb}} = 0$ then the probe is actually floating, i.e. the reference potential is chosen to be the floating potential (in contrast to equation 3.15). Finally, expression 4.10 is the actual synthetic IV characteristic of the target single Langmuir probe. This can be processed in the same way than a regular experimental IV characteristic and this is how the synthetic T_e is deduced. The results obtained for various input profiles will be presented in chapter 5.

4.5 Estimates of the mean free path used in the simple model

One of the principal goals of this thesis was to do a search for a more accurate formula for the mean free path and to try and implement them in the simple model. A general method of how to derive collisional parameters in a plasma will be outlined in this section, along with several possibilities how to calculate the mean free path of an electron in a plasma.

4.5.1 Fokker-Planck equation

The collision frequency in a plasma is not as straightforward to define as in a neutral gas. A charged plasma particle undergoes elastic Coulomb collisions. The Coulomb interaction in principle can act at an infinite range, however the shielding effect of the plasma causes that any particle effectively interacts only with particles within its Debye sphere. Collisions are not binary, the particle weakly interacts with many other particles at once rather than with one dominating particle passing close by.

The plasma collision frequency and also other collisional parameters characterizing relaxation processes in a plasma can be calculated from the Fokker-Planck equation. The Fokker-Planck equation is in fact a special case of the more general Boltzmann transport equation, which is an equation for the distribution function for a specific particle species characterized by mass m and charge state Z:

$$\frac{\partial f}{\partial t} + \mathbf{v}.\nabla_{\mathbf{x}} f + \frac{\mathbf{F}}{m}.\nabla_{\mathbf{v}} f = \left(\frac{\partial f}{\partial t}\right)_{\mathrm{col}} \tag{4.11}$$

The right hand side of this equation is the collision term, which for the Fokker-Planck equation is equal to (according to the Rosenbluth derivation):

$$\left(\frac{\partial f}{\partial t}\right)_{\mathrm{col}} = -\alpha \frac{\partial}{\partial \mathbf{v}}. \left(f \frac{\partial H}{\partial \mathbf{v}}\right) + \frac{1}{2}\alpha \frac{\partial^2}{\partial \mathbf{v} \partial \mathbf{v}} : \left(f \frac{\partial^2 G}{\partial \mathbf{v} \partial \mathbf{v}}\right), \tag{4.12}$$

where

$$\alpha = \frac{Z^2 e^4}{4\pi \epsilon_0^2 m^2} \mathrm{ln} L,$$

$\mathrm{ln}L$ is the Coulomb logarithm, ":" denotes tensor multiplication and H, G are the *Rosenbluth potentials*:

$$H = \sum_s Z_s \left(\frac{m + m_s}{m_s}\right) \int \frac{f_s(\mathbf{v}_s)}{|\mathbf{v} - \mathbf{v}_s|} \mathrm{d}\mathbf{v_s} \tag{4.13}$$

$$G = \sum_s Z_s^2 \int |\mathbf{v} - \mathbf{v}_s| f_s(\mathbf{v}_s) \mathrm{d}\mathbf{v_s} \tag{4.14}$$

These functions represent the coulomb interaction between the particle species of interest (with distribution function f) and the other particle species (including the interaction with themselves, i.e. self-interactions), denoted by index "s" and characterized by distributions, masses, charge states f_s, m_s, Z_s respectively. A derivation of the Rosenbluth potentials can be found in [34]. Next, it will be shown how various collisional parameters can be derived.

4.5.2 The test particle model

By computing velocity moments of the Fokker–Planck equation we may define and find estimates for various collisional parameters (relaxation times, collision frequencies, mean free paths) for different processes in the plasma [34]. A very simple model that permits the calculation of rough estimates of such quantities is the test particle model in which a single test particle (either an electron or an ion) travels through a uniform, field-free plasma in thermal equilibrium. This is called the *test particle model*. In this case, spatial derivatives disappear and $\mathbf{F} = 0$ thus the Fokker–Planck equation is simply:

$$\frac{\partial f}{\partial t} = -\alpha \frac{\partial}{\partial \mathbf{v}}. \left(f \frac{\partial H}{\partial \mathbf{v}}\right) + \frac{1}{2}\alpha \frac{\partial^2}{\partial \mathbf{v} \partial \mathbf{v}} : \left(f \frac{\partial^2 G}{\partial \mathbf{v} \partial \mathbf{v}}\right). \tag{4.15}$$

The distribution of the test particle (a beam of test particles) with velocity $\mathbf{V}$ is a delta function:

$$f(\mathbf{v}, t) = \delta(\mathbf{v} - \mathbf{V}(t)) \tag{4.16}$$

where $\mathbf{V}(t)$ is the particle velocity at time t and we find estimates for various collisional parameters by evaluating the velocity moments at $t = 0$.

Friction

Let us substitute expression 4.16 into 4.15 and compute the $\mathbf{v}$ moment of equation 4.15 (i.e. applying operator $\int \mathbf{v} \cdot (...)\mathrm{d}\mathbf{v}$). The resulting equation is:

$$\frac{\partial \mathbf{V}}{\partial t} = \alpha \frac{\partial H(\mathbf{V})}{\partial \mathbf{V}} \tag{4.17}$$

Next, a Maxwellian distribution for the field particles will be assumed:

$$f(\mathbf{v}_s) = \left(\frac{m_s}{2\pi k T_s}\right)^{3/2} \exp\left(-\frac{m_s \mathbf{v}_s^2}{2kT_s}\right). \tag{4.18}$$

After integrating through $\mathbf{v}_s$ the following equation is obtained:

$$\frac{\partial \mathbf{V}}{\partial t} = -\frac{\mathbf{V}(t)}{\tau_{\mathrm{f}}(\mathbf{V})} \tag{4.19}$$

where τ is the characteristic time for the loss of velocity in the direction of $\mathbf{V}(0)$. In a sense it can be regarded as the mean time that the velocity in the direction of $\mathbf{V}(0)$ decreases to 1/e of its original value. However, this holds only in the close vicinity of V, since $\tau_{\mathrm{f}} = \tau_{\mathrm{f}}(V)$. The inverse of this relaxation time τ_{f} is the frictional coefficient ν_{f}:

$$\nu_{\mathrm{f}} = \frac{1}{\tau_{\mathrm{f}}} = \frac{2\alpha}{V} \sum_s Z_s^2 \left(\frac{m + m_s}{m_s}\right) n_s a_s^2 \Psi(a_s V) \tag{4.20}$$

and $a_s = \sqrt{(m_s/2kT_s)}$. Ψ is the Chandrasekhar function,

$$\Psi(x) = \frac{\mathrm{Erf}(x) - x\mathrm{Erf}'(x)}{2x^2}. \tag{4.21}$$

The parameter ν_{f} describes the rate of change of the particle velocity in a plasma due to friction (i.e. slowing down of the particle velocity in its original direction). It is visible from expression 4.20 that the collisions are more effective for higher density and less effective for higher temperature.

Other moments can be calculated to obtain collisional parameters for other processes. Let us have a look at two more processes:

Deflection through a right angle

Here, the $v_\perp^2$ moment of the distribution function is calculated, where $v_\perp^2$ is the sum of the squares of the components of $\mathbf{v}$ perpendicular to $\mathbf{V}(0)$. The equation deduced from the test particle model is [34]:

$$\frac{\partial V_\perp^2}{\partial t} = \frac{V^2(t)}{\tau_\perp}, \tag{4.22}$$

where $\tau_\perp$ is the mean time it takes a particle to be deflected through a right-angle. The inverse of this time is, by definition, the *collision frequency* in a plasma for an arbitrary particle species:

$$\nu_\perp = \frac{1}{\tau_\perp} = \frac{2\alpha}{V^3} \sum_s Z_s^2 n_s \left(\mathrm{Erf}(a_s V) - \Psi(a_s V)\right) \tag{4.23}$$

Energy exchange

Let W be the energy of the test particle and $\Delta W =$ and we take the $\Delta W^2 = (W(t) - 1/2mV^2(0))^2$ the square of energy transfered to the plasma (i.e. lost by the particle) as the moment of 4.15. This, according to [34] represents the process of energy exchange. The calculation yields the equation

$$\frac{\partial(\Delta W)^2}{\partial t} = \frac{W^2(t)}{\tau_\mathrm{E}}. \tag{4.24}$$

The characteristic time for energy exchange defines another collisional parameter:

$$\nu_\mathrm{E} = \frac{1}{\tau_\mathrm{E}} = \frac{8\alpha}{V^3} \sum_s Z_s^2 n_s \Psi(a_s V). \tag{4.25}$$

4.5.3 Mean free path

From the collisional parameters, the mean free paths for the respective processes can be simply evaluated by expression:

$$\lambda(V, n_e, T_e) = \frac{V}{\nu(V, n_e, T_e)}, \tag{4.26}$$

i.e. by dividing the particle velocity by the collision frequency for the respective process.

By considering only e-e self-collisions ($m = m_e = m_s$, $Z = Z_s = 1$, $T_s = T$ $n_s = n_e$) and using equation 4.5 we obtain the expressions for the mean free path for the different collisional processes. The mean free path as a function of the velocity is plotted in 4.4 for electron density $n_e = 10^{20}$ m^{-3} and temperature $T_e = 10$ eV, which are typical values for a high density SOL plasma.

In chapter 5, result for all of these expressions for the mean free path will be shown.

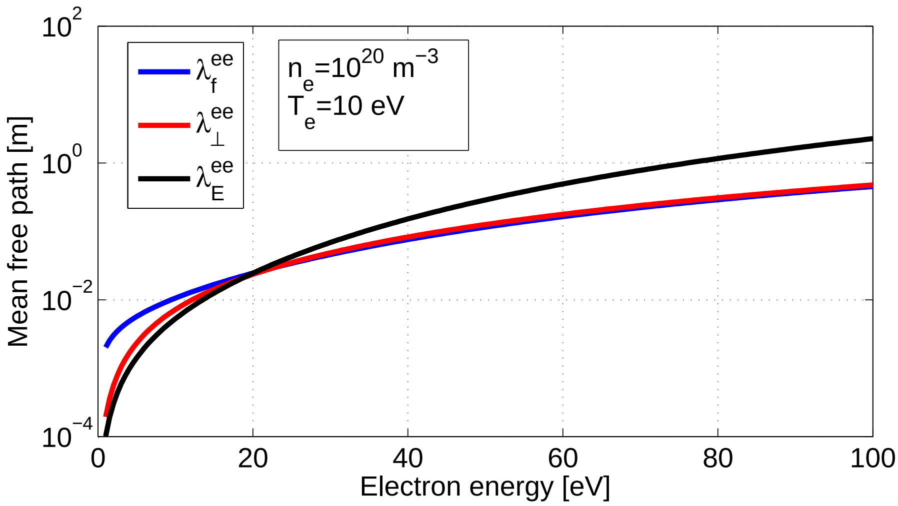

Figure 4.4: The mean free paths for electrons moving in a Maxwellian field of electrons with $n_e = 10^{20}$ m^{-3} and $T_e = 10$ eV for friction (blue), deflection through a right angle (red) and energy exchange (black) as a function of the electron energy. Logarithmic plot.

Chapter 5

Results

In this section, results obtained from the model decribed in sections 4.3, 4.4 and 4.5 will be presented and interpreted for JET input data. For TCV data, this has been done within my bachelor thesis [11].

5.1 Typical results

5.1.1 Synthetic EVDFs & IV characteristics

In this section, EVDFs calculated for the individual density cases described in 4.2 will be presented. Each density case will be represented by typical T_e and n_e profiles used to calculate the EVDF. These profiles are depicted in Fig. 5.1.

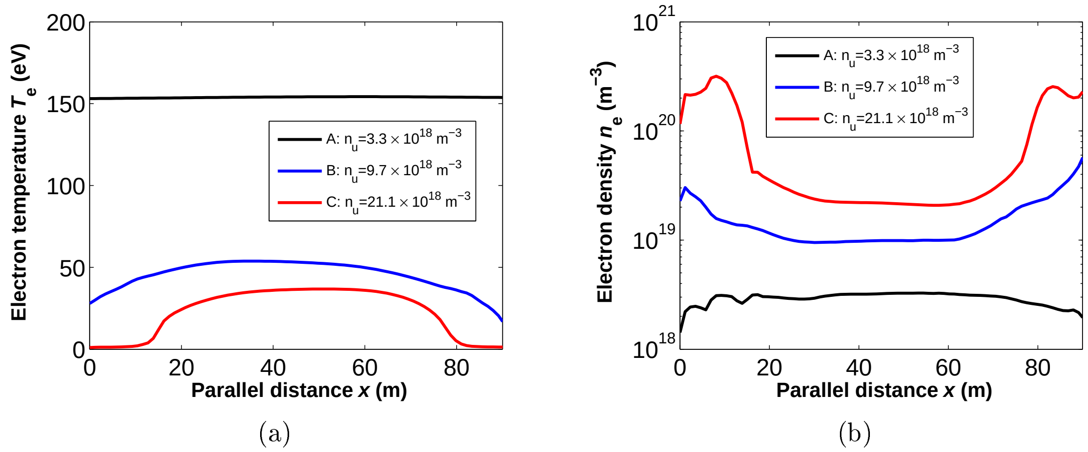

Figure 5.1: Typical T_e (a) and n_e (b) profiles representing the various density regimes. $x = 0$ is the outer divertor.

The IV characteristic is calculated from the distribution function as described in section 4.4 in a range of voltages pertinent to a real situation, from -100 V to floating potential or slightly more. Next, the computed characteristic is fitted by equation 3.11 in order to obtain the electron temperature, just like as if it were experimental data. Assuming our model is correct, this is the temperature that a probe inserted in the given plasma is supposed to measure. For results presented within this section, the mean free path for energy transfer was used.

Sheath limited regime (Low density case)

A typical result for the low density case (see section 4.2) for the profile A from Fig. 5.1 is shown in Fig. 5.2(a). In the sheath limited regimes, there is no T_e gradient, thus the target EVDF is the same as the upstream EVDF. No distortion in the synthetic EVDF is visible (i.e. it is Maxwellian), which is what we would expect.

The same holds for the IV characteristic in Fig. 5.2(b). The synthetic IV characteristic from the simple model is identical to the IV characterstic calculated by formula 3.15 from the temperature that would correspond to the EDGE2D-EIRENE predicted target T_e.

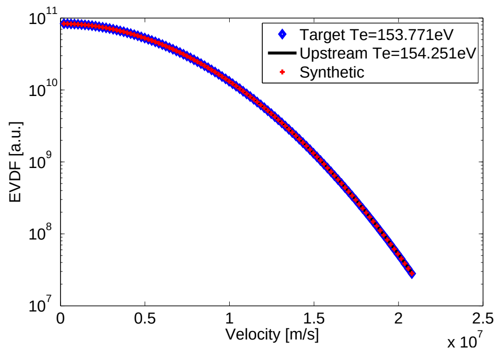

(a)

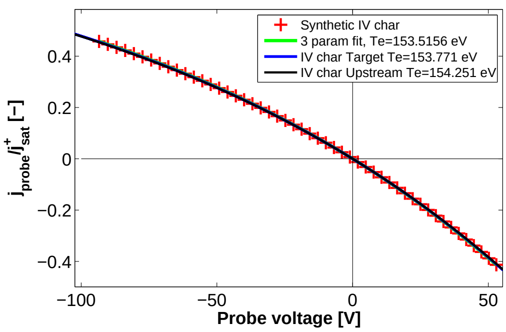

(b)

Figure 5.2: **Low density case**: (a) Synthetic EVDF (red) computed by the model, Maxwellian EVDF (blue) at the outer divertor target and Maxwellian upstream EVDF (black). The synthetic EVDF is calculated for EDGE2D-EIRENE profile A (Fig. 5.1) and the Maxwellian at the target is calculated for $T_e(0)$ (Given by EDGE2D-EIRENE).
(b) Synthetic IV characteristic computed from the synthetic EVDF in 5.2(a). 3-paramter fit of the synthetic IV characteristic (green) and IV characteristic corresponding to the target (blue) and upstream (black) T_e from EDGE2D-EIRENE. The IV characteristic is shifted so that $V_{\text{fl}} = 0$.

Medium density case (High recycling regime)

For the high recycling regime, a significant temperature gradient is present. A typical EVDF is computed from profile B from Fig. 5.1. The target and upstream EVDFs deduced from EDGE2D-EIRENE clearly have a different temperature, with the upstream being higher. The EVDF for the high recycling case is visualized in Fig. 5.3(a).

It can be seen that the bulk of the EVDF is the same as the target EVDF deduced from EDGE2D-EIRENE, while the tail is enhanced and somewhat resembles the upstream EVDF computed by EDGE2D-EIRENE, representing a population of hot upstream electrons. Hence, for this case, we have obtained a non-Maxwellian distribution for target electrons from the simple model.

Consequently, the IV characteristic is not identical to the IV characteristic corresponding to the EDGE2D-EIRENE prediction of $T_e(0)$ anymore. Instead, it lies between the target IV characteristic and the IV characteristic that corresponds to the higher upstream temperature, Fig. 5.3(b). As a consequence, a 3-parameter fit of the synthetic IV characteristic yields a higher temperature, 33 eV instead of the 28 eV which is the temperature of the bulk of the distribution.

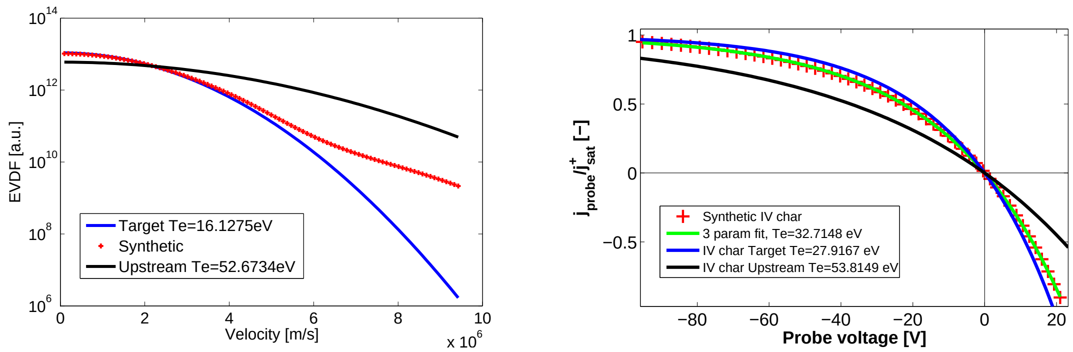

(a) (b)

Figure 5.3: **Medium density case**: (a) Synthetic EVDF (red) computed by the model, Maxwellian EVDF (blue) at the outer divertor target and Maxwellian upstream EVDF (black). The synthetic EVDF is calculated for EDGE2D-EIRENE profile B (Fig. 5.1) and the Maxwellian at the target is calculated for $T_e(0)$ (Given by EDGE2D-EIRENE). Two distinct populations of electrons are visible for the synthetic EVDF, one bulk electron population and a fast electron component, originating in hotter upstream region of the T_e profile for the HRR.
(b) Synthetic IV characteristic computed from the EVDF in Fig. 5.3(a). The color code is the same as in Fig. 5.2(b).

Partially detached regime (High density case)

Similarly to the HRR, the partially detached regime also has T_e gradients, thus one would expect that the EVDF for this case will also be distorted, causing the probes to overestimate T_e. A typical EVDF for the partially detached regime, computed from T_e and n_e profiles corresponding to a partially detached $n_u = 21.1 \times 10^{18}$ m^{-3}, can be seen on Fig. 5.4(a). The temperature drop in the SOL is significant for this case, the upstream T_e being ~ 40 times higher than the target T_e.

Surprisingly, no distortion of the EVDF is predicted for this case, which means that the IV characterstic is the same as the one computed from the target T_e from EDGE2D-EIRENE. Consequently, no temperature overstimation by probes is predicted.

The question that arises is the following: Why does the partially detached regime give a qualitatively different result than the HRR, if the T_e profiles are similar? To find the answer, we must have a look at the n_e profile.

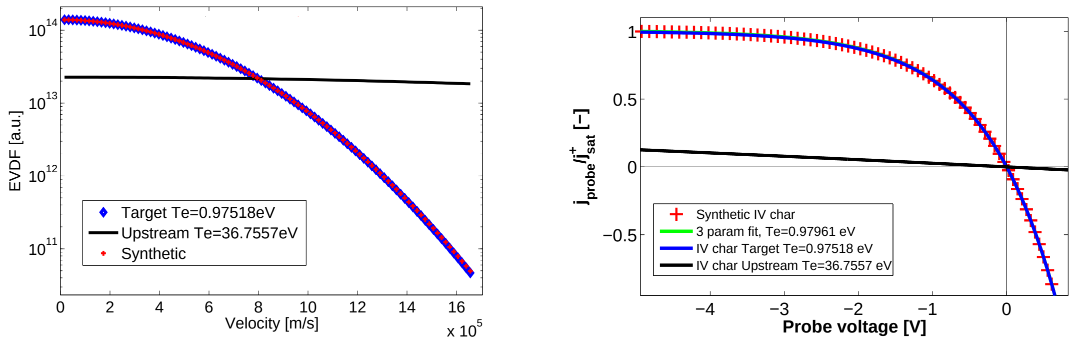

(a) (b)

Figure 5.4: **High density case**: (a) Synthetic EVDF (red) computed by the model, Maxwellian EVDF (blue) at the outer divertor target and Maxwellian upstream EVDF (black). The synthetic EVDF is calculated for EDGE2D-EIRENE profile C (Fig. 5.1) and the Maxwellian at the target is calculated for $T_e(0)$ (Given by EDGE2D-EIRENE). The synthetic EVDF at the target is not distorted..
(b) Synthetic IV characteristic computed from the EVDF in Fig. 5.4(a). The color code is the same as in Fig. 5.2(b).

The reason for this unexpected behaviour is believed to be in the very high density in the divertor region for this case. The mean free path even for fast electrons is very low, thus the large density peaks in the divertor region can be regarded as "barriers" for the supra thermal electrons originating upstream. As they cannot penetrate into the divertor region, they do not affect the target EVDF. Only extremely high energy electrons can overcome this barrier, however these are not at all numerous due to the form of the Maxwellian distribution function.

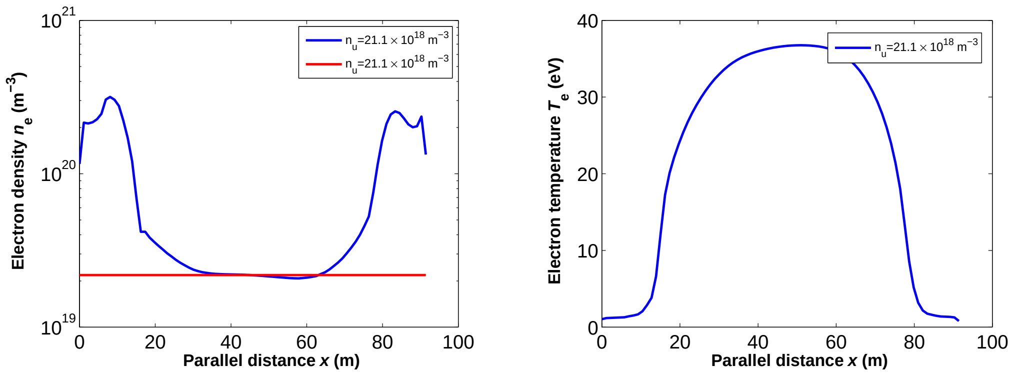

(a) (b)

Figure 5.5: (a) The newly defined flat n_e profile compared to the original n_e profile corresponding to C. In upstream locations the original and modified profiles are similar. (b) The T_e profile used in the synthetic experiment, corresponding to the unmodified density profile from EDGE2D-EIRENE.

The effect of the high density barriers described in the previous paragraph can be demonstrated by the following synthetic experiment. The density profile labeled C is redefined as a flat profile where the n_e is has the constant value of the upstream density. From Fig. 5.5(a) we see that this choice of the n_e profile virtually levels out the density barriers at the divertor regions.

If we run the simple model for such a modified input, the code predicts a distorted EVDF and overestimation by probes a factor of $\sim$ 10.This analysis supports the hypothesis that the density peaks at the divertors prevent fast electrons from reaching the target.

5.2 Effect of various expressions for the mean free path

In this section, the results of the model will be presented for mean free paths for various collisional processes described in section 4.5. The result of the model for each mean free path will be summarized in a *density scan*. In each density scan, every input profile from 4.2 is analyzed and the result plotted in one figure.

In principle, one could put the results for the various mean free paths into one density scan. In practice, however, this would mean that the figure would become overpopulated by a number of very similar curves, since the results for the various mean free path are very similar, as we shall see. Hence, the density scans for the three mean free paths will be plotted in separate viewgraphs, 5.6 (a), (b) and (c).

From Fig. 5.6 (for the outer target) it can be seen that each of the expressions for the mean free path gives qualitatively the same result. For low (sheath limited) and high (partially detached) density regimes, the simple model predicts that probes should measure the correct T_e. For the medium density regime, the model predicts that probes should measure a somewhat higher temperature (up to 20%) higher than they should. The effect is most visible for the largest mean free path, which is $\lambda_{\mathrm{E}}^{ee}$, i.e. for energy transfer.

The situation is the same for the inner target as well. This is not at all surprising, since the input parallel T_e and n_e profiles are roughly symmetric.

From now on, the mean free path used in subsequent section will be exclusively the one for energy exchange, since this is the one when the effect of overstimation is most visible.

5.3 Effect of the fitting method

It was found that the fitting method also has an appreciable effect on the probe T_e prediction by the simple model. To demonstrate this, old TCV input data from my bachelor thesis were used, since the effect is much better visible. The effect is also visible for JET but at a smaller scale, not suitable for visualisation.

Input profiles for TCV were generated by the B2-EIRENE code (SOLPS) wich virtually uses the same physics as EDGE2D-EIRENE. In principle, the profiles for the various density regimes are qualitatively similar than the ones shown in section 4.2.

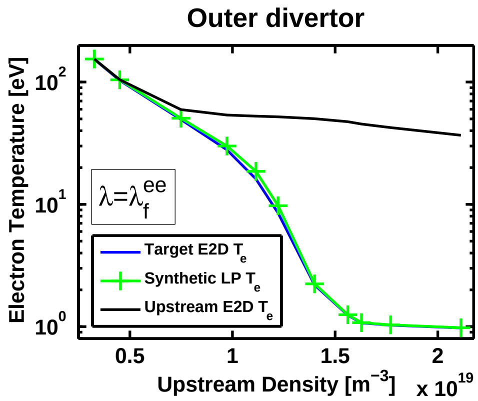

(a)

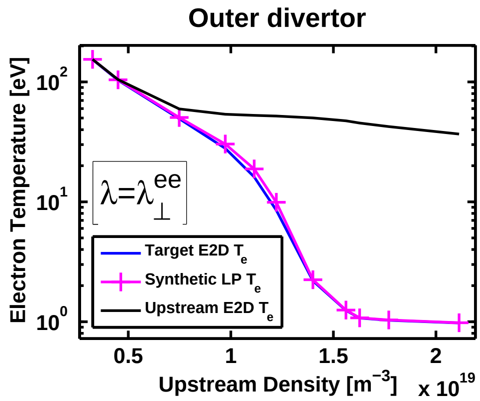

(b)

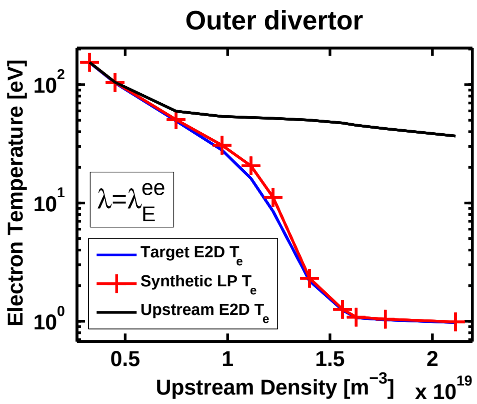

(c)

Figure 5.6: Density scans for each expression for the mean free path for the outer target. (a) Mean free path for friction, (b) Deflection over a right angle, (c) Energy exchange. In each density scan, the synthetic temperature is plotted as a function of the upstream density, which characterizes the T_e and n_e profiles used as input to calculate it. For comparison, the corresponding target and upstream T_es from EDGE2D-EIRENE are also plotted.

Simulations for TCV thus yielded a similar result - T_e overestimation is visible only for the HRR. The most notable difference in the TCV profiles is in the connection length - being shorter by a factor of ~ 2 at TCV, since it is a smaller tokamak. This means that the T_e gradient is steeper, leading to a more significant overestimation effect, up to a factor of ~ 1.8, as seen in Fig. 5.7 for the 3-parameter fit. It is found that if the 4-parameter fit is used to obtain T_e from the synthetic IV characteristic, the overestimation effect is less significant.

To find the reason for this, it is illuminating to plot the synthetic IV characteristic for a HRR together with the 3-parameter and 4-parameter fits, Fig. 5.8. The non-Maxwellity of the synthetic distribution function leads to an IV characteristic that is not of the form given by expression 3.15, but is a combination of the IV characterstic representing the bulk and an IV characteristic representing the tail of the EVDF. For such an IV characteristic, a 3-parameter fit does not fit the data well, Fig. 5.8.

On the other hand, the 4-parameter fit yields a significantly better fit. It appears

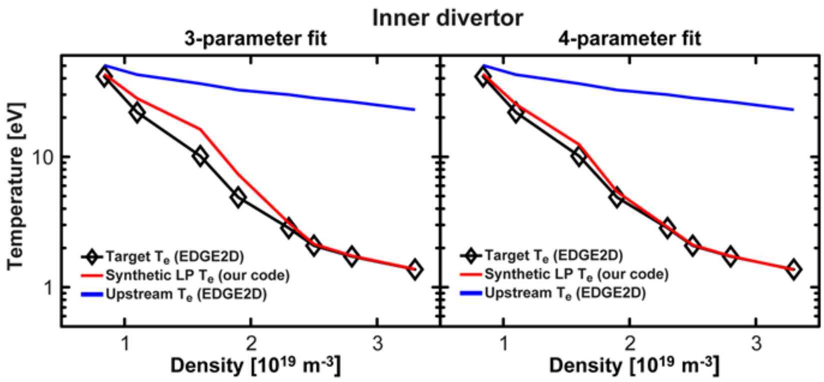

Figure 5.7: Density scans for TCV for 3-parameter and 4-parameter fits.

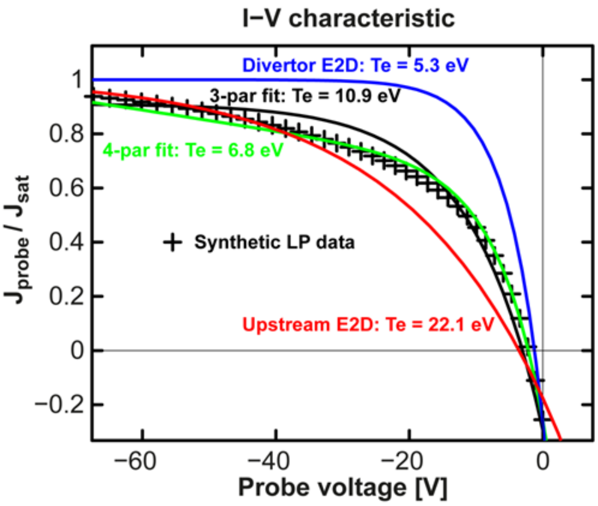

Figure 5.8: Synthetic IV characteristic and its corresponing 4-parameter and 3-paramter fits for a HRR for input data from TCV.

that the effect of hot electrons on IV characteristic is similar to the sheath expansion effect, which is treated by 4-parameter fit. As a result, use of 4-parameter fit itself significantly reduces effect of hot upstream electrons on T_e deduced from fitting the IV characteristic.

5.4 Comparison to single probe data

5.4.1 JPN 81469-81482 density ramps

In this section, results will be compared to experimental probe measurements from the JET divetor Langmuir probe diagnostic, KY4D. The poloidal layout of the probes can be seen in Fig. 5.9. For shots from Exp-3.1.2 (JPNs 81469-81484), the inner strike point was on the inner vertical target, while the outer strike point was situated at the horizontal target. In Fig. 5.10 one can see how the actual probes look like compared to the horizontal divertor targets. The probes can be configured to operate either as triple probes or swept single probes. In this experiment, all functional probes were operated as single probes, which is convenient since our model calculates synthetic IV characteristics for single probes, making the comparison easier.

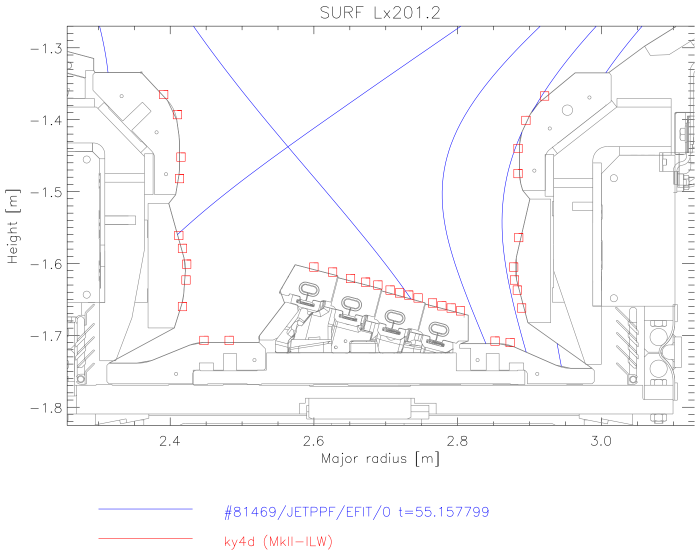

Figure 5.9: Layout of the JET divertor Langmuir probe system, KY4D.

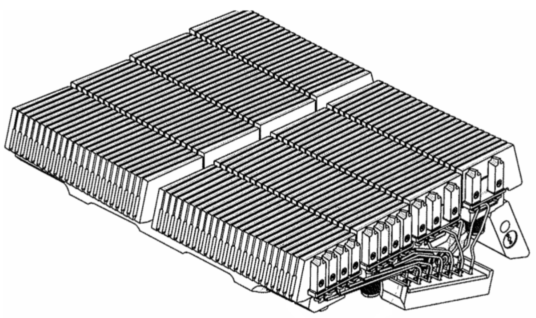

Figure 5.10: Illustration of JET divertor Langmuir probes at the horizontal target plate.

The data comprises radial target T_e profiles for several density cases. In Fig. 5.12 target radial profiles for the three typical density cases are shown, again a low (SL), intermediate (HRR) and high density case (PD) were used for the comparison. This kind of spatially resolved data can be experimentally aquired by local sweeping of the strike points. The peak at position (roughly) $R - R_{\mathrm{sep}} = 0$ is the strike point. The description of pulses from which the LP data comes from is in Tab. 5.1.

Once we have the LP data, we can finally do the comparison. The nature of the comparison is not so straightforward since we have probe data corresponding to several shots from within Ex. 3.1.2. (JPNs 81472, 81480, 81484) and our synthetic T_e is calculated from simulations for JPN 81469. These shots all had similar machine settings.

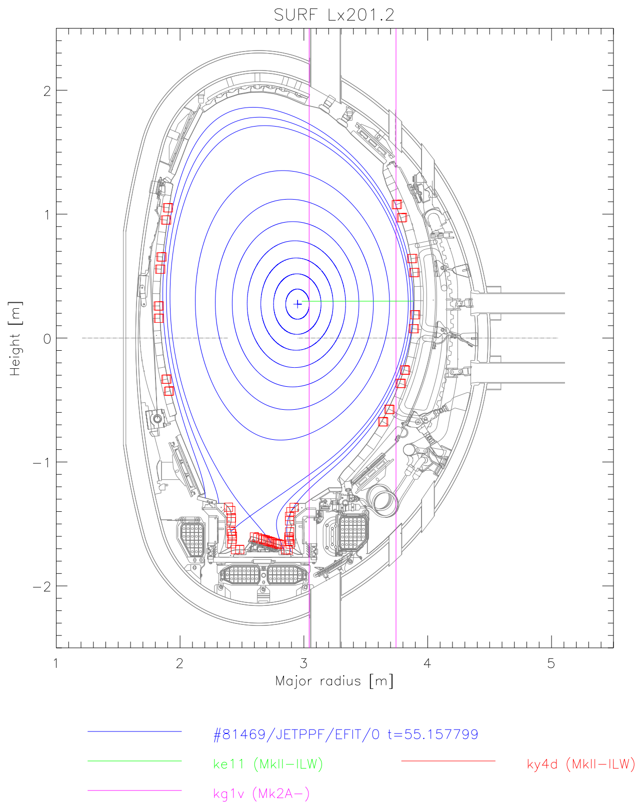

Figure 5.11: JET poloidal cross-section with magnetic equilibrium (blue), the high resolution Thomson scattering line of sight (KE11, green), vertical interferometry chords (KG1V, magenta) and Langmuir probes (KY4D, red).

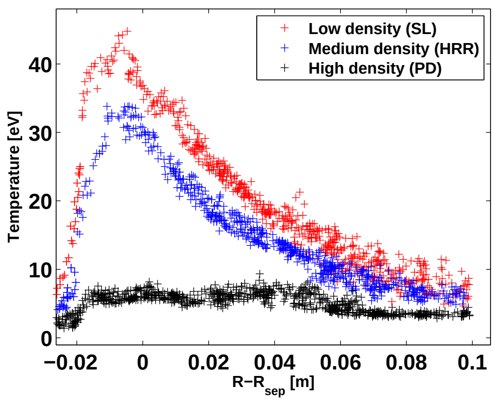

Figure 5.12: An example of spatially resolved experimental divertor single probe data. The plot displays the temperature at the divertor measured by probes as a function of the separatrix distance, mapped to the outer midplane separatrix.

What we want to do is populate a density scan with real experimental data. Hence, we must determine the experimental T_e for the flux surface of interest, which is the flux surface 5 mm from the separarix (mapped to the outer midplane). As for

Density case	JPN	Time	$n_{e,sep,omp}$ (HRTS)	$n_{e,lav}$ (KG1V/LID4)
Low (SL)	81472	50 s	0.8×10^{-19} m^{-3}	1.15×10^{-19} m^{-3}
Medium (HRR)	81484	50 s	1.05×10^{-19} m^{-3}	1.77×10^{-19} m^{-3}
High (PD)	81484	53 s	1.75×10^{-19} m^{-3}	2.95×10^{-19} m^{-3}

Table 5.1: Description of the experimental LP data plotted in Fig. 5.12 including the pulse number, time into the pulse, corresponding outer midplane separatrix (electron) density from high resolution Thomson scattering ($n_{e,sep,omp}$) and line averaged edge density ($n_{e,lav}$) from interferometry.

the density to assign to a probe measurement, we take the corresponding midplane separatrix density from HRTS, or alternatively the line averaged edge density from interferometry. The corresponding densities for the three profiles from Fig. 5.12 are in Tab. 5.1.

Now we need to plot the synthetic temperatures from the simple model as a function of the midplane separatrix (from EDGE2D-EIRENE). The difference between the midplane separatrix density and upstream density (which was used in density scans up to now) is not much since the SOL width is typically in the order of cm. Nevertheless, it is more correct to do it this way. A density scan created this way is given in Fig. 5.13.

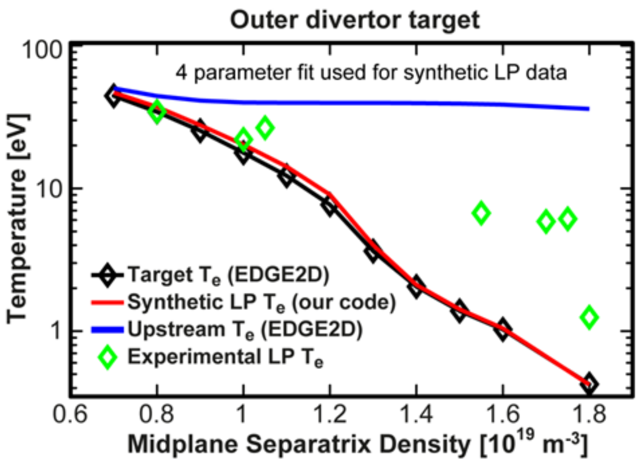

Figure 5.13: Comparison of EDGE2D-EIRENE predicted target T_e (black), synthetic temperature that the probes would hypothetically measure from the simple model (red) and the experimental LP measured temperature (green).

From Fig. 5.13 it is visible that for the low density case, the experimental measurement is in good accordance whith EDGE2D-EIRENE. This is consistent with the fact that our model does not predict overestimation for this density region.

For the medium density region there is almost no data available, except one data point at $n_{\mathrm{e,sep,omp}} = 1.05 \times 10^{19}$ m^{-3}. The probe overestimates T_e by a factor of $\sim$1.5 compared to the target EDGE2D-EIRENE prediction. The simple model does predict overestimation for this case, however only in the range of several %.

The region of the biggest interest is the high density region corresponding to partial detachment of the target. The probes really overestimate T_e significantly for this case compared to EDGE2D-EIRENE (and as frequently reported, see section 4.1), by factor of up to $\sim$10.

To make sure whether this also holds for all the radial positions, we have made a radial comparison of the result fo the simple model, EDGE2D-EIRENE target predictions and the experimental data. This is shown in Fig. 5.14 and as wee see looking at different radial position does not bring any surprises, the EDGE2D-EIRENE predicted temperature is by factors of 10 lower than the experimental measurement. The simple model does not predict overestimation for any of the radial positions.

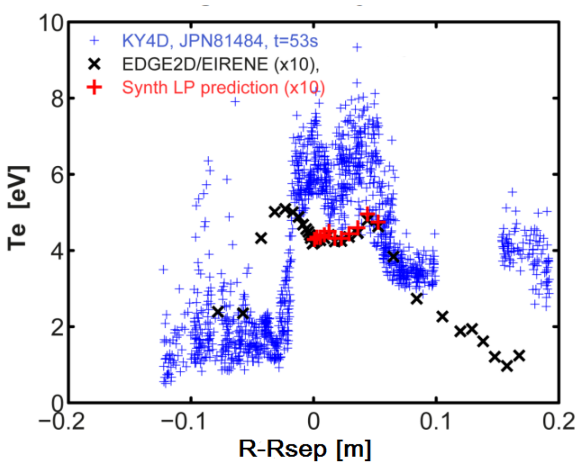

Figure 5.14: Radial comparison of the experimental probe temperature, the EDGE2D-EIRENE target prediction and the simple model prediction (the latter two multiplied by 10 for better visibility) for the outer target for a partially detached case corresponding to $n_{\mathrm{e,sep,omp}} = 1.75 \times 10^{19}\ \mathrm{m}^{-3}$.

For the high density case, our model does not predict temperature overestimation by probes (for the reason desrcibed in section above), but the experimental probe data seem to be overestimated. This preliminary comparison suggests that the steep parallel temperature gradients are not the main cause of Langmuir probes overestimating the divertor temperature. This result is tentatively suggested also in paper [13].

5.4.2 Density ramp JPN 82342

JET pulse number 82342 was also a density ramp discharge very similar to the discharges used in the previous section. In Fig. 5.15(b), one can see four typical density cases for the flux surface 1.3 mm from the separatrix.

In this discharge, there was no strike point sweep, i.e. the data shown here are from just one single probe corresponding to the respective flux surface. Experimental T_e shown here was aqcuired via the 4-parameter fit from the experimental characterstics.

However, for the input profiles in Fig. 5.15(b), the simple model predicts that hot upstream electrons should not affect divertor LP T_e measurements assuming (using

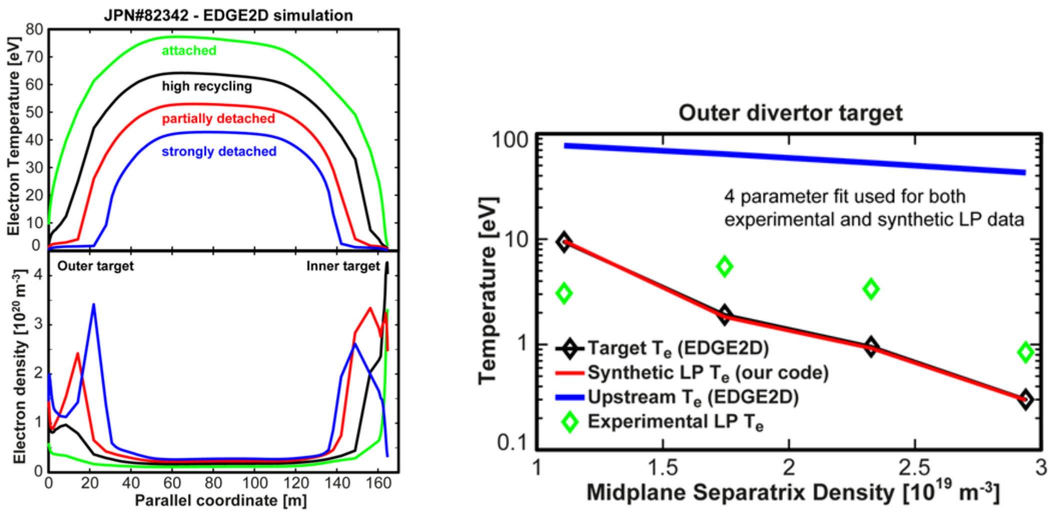

(a) (b)

Figure 5.15: (a) Parallel T_e and n_e input profiles from EDGE2D-EIRENE for several density cases. The case labeled "attached" is a medium density case. (b) Density scan with experimental data for the outer target. The 4-parameter fit was used to obtain T_e from both experimental and synthetic IV characteristics.

the 4-parameter fit), which is visible from Fig. 5.15. The reason is a connection length that is roughly 2 times higher than for the profiles shown in section 4.2.

It is important to note that with the 4-parameter fit, the discrepancy between the EDGE2D-EIRENE prediction and the experimental T_e is not so significant, typically, probes tend to overestimate only by a factor of up to $\sim$3.

5.5 Comparison of the simple model to the BIT1 parallel PIC code

In this chapter the simple model is compared to the result of a complex PIC code with the intention of benchmarking. Data are currently available from the BIT1 kinetic code [14]. The code computes a number of quantities, including the T_e and n_e profiles. Additionally, as it is a kinetic code, the distribution functions, not necessarily Maxwellian, are also calculated. In fact, whole profiles of EVDFs are available. This would pose a problem for the computation of the electron mean free path, as it could not be calculated by the simple formula anymore (the simple formula assumes maxwellian distribution). The mean free path is an average quantity, thus integration over each distribution (general, non-Maxwellian) should be done during each step. This would raise additional computational requirements that would possibly not be reasonable any more.

In paper [14] a BIT1 simulation is performed for stationary SOL conditions as well as for ELMs. The key player of the simulation is the ratio of elastic and inelastic collisions. In Fig. 5.16 calculated distribution functions for different collisionalit-

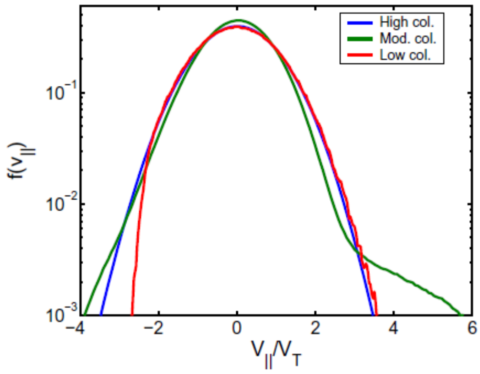

Figure 5.16: Normalized EVDFs at the position of a triple Langmuir probe for stationary SOL with different collisionalities. [14]

ies and SOL regimes are shown. Electron collisionality ν^* is defined as the ratio of electron-electron collision frequency and the electron bounce frequency. The bounce frequency is that at which electrons trapped on banana orbits oscillate. BIT1 predicts a non-Maxwellian EVDF for the moderate collisionality case. The moderate collisionality case can be considered to correspond to a medium density (HRR). For this case, we have obtained outputs from the BIT1 code, namely:

- Electron and ion VDFs along the whole SOL parallel profile.
- Parallel T_e and n_e calculated directy from the EVDFs.

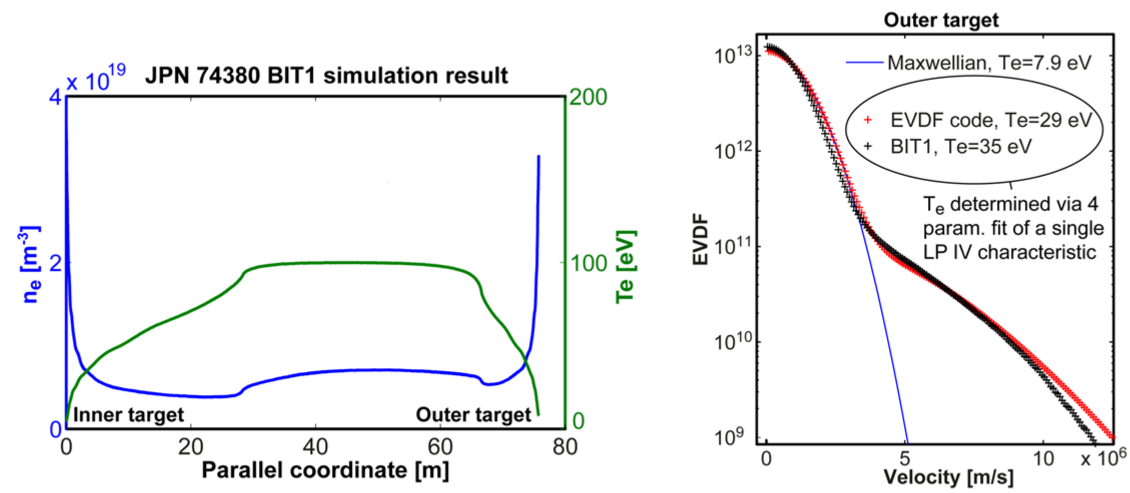

(a) (b)

Figure 5.17: (a) Parallel T_e and n_e input profiles computed by BIT, corresponding to a HRR. (b) Outer target EVDFs from BIT1 (black), the simple model using input profiles from Fig. 5.17 (a) and a Maxwellian EVDF for T_e computed from the BIT1 EVDF.

Hence we can use the T_e and n_e profiles deduced from BIT1 EVDFs and then compare our computed target EVDF to the target EVDF from BIT1. The T_e and n_e profiles are in Fig. 5.17(a).

It is found that the target EVDFs for the high recycling regime from BIT1 and from the simple model are both non-Maxwellian, Fig. 5.17(b). However, they are very similar, both with a dominant bulk of thermanl electrons and a significant population of hot electrons at the tail of the EVDF. Both EVDFs also yield similar synthetic probe T_e measurements, as depicted in Fig. 5.17(b). Since agreement between BIT1 and the simple model target EVDF has been found, this suggests that the simple model might be a valuable tool to predict target EVDFs provided that the input profiles are specified, e.g. by EDGE2D-EIRENE, SOLPS etc.

Chapter 6

Summary

This diploma thesis is a natural continuation of my bachelor thesis and research project. The main objectives of the diploma thesis were to:

(a) Further improve the model for computing divertor target electron distribution functions.

(b) Perform a detailed comparison of Langmuir probe T_e as predicted by the simple model to real experimental data from JET divertor LPs.

(c) Compare results from the simple model to available kinetic PIC codes.

(d) Formulate conclusions concerning the applicability of the simple model to simulate real divertor target EVDFs.

In the first chapter of the thesis, introduction to nuclear fusion and magnetic confinement is given and the JET tokamak is introduced. In the second chapter, basic theory on divertor physics and divertor operating regime is given and also an overview of relevant plasma surface interactions is provided. The EDGE2D-EIRENE fluid code is introduced, since it is the main source of input data for the simple EVDF model. In chapter three, basic principles of Langmuir probe operation is given, with description of single, double and triple probes and their advantages/disadvantages. Two distinct fitting methods are desrcibed in the case of the single probe, the 3-parameter fit and the 4-parameter fit. The latter is an extension to the treatment of synthetic IV characteristics and can in a sense be considered as one of the improvements to the code in the frame of objective (a).

In chapter four, the issue of Langmuir probe T_e overestimation at divertor targets is discussed. The simple kinetic model is thoroughly introduced and desribed with the amendments that have been done in the frame of the diploma thesis. This model comprises of the calculation of EVDFs at the divertor targets using parallel SOL profiles of T_e and n_e generated by the EDGE2D-EIRENE fluid code. Synthetic Langmuir probe IV characteristics are then computed from the EVDFs. The value of the electron temperature is determined from these synthetic IV characteristics in the same way as from experimental Langmuir probe data. The major improvements done in the code was the introduction of a variable step length computed as a fraction of the local value of electron mean free path and using a more appropriate formula for the construction of the target EVDF. Additionally, a considerable part of this chapter is devoted to the derivation of various estimates of the electron mean free path in a plasma and the various estimates for the mean free path are subsequently tested. In the bachelor thesis, a very rough estimate was used. Nevertheless, it is found that all of the estimates of the mean free path give qualitatively the same results.

Lastly, in chapter five, simulation results for JET input data (and marginally also for TCV) are presented. It is found that if significant parallel temperature gradients are present, the target EVDF can be significantly distorted, more precisely, the tail of the distribution function is enhanced, which afterwards leads to overestimation of Langmuir probe measurements. The simulations predict the following:

1. For low density divertor regimes, i.e. the sheath limited regime, probes should measure correctly. Explanation: T_e and n_e gradients are not present in these cases.

2. For medium densities, i.e. typically high recycling regimes, a weak overestimation of factor up to 20% is predicted. Explanation: Large T_e gradients, n_e profile fairly flat.

3. For high densities, i.e. for the partially detached and detached case, no overestimation is predicted, i.e. probes should measure correctly. Explanation: Large T_e gradient but in contrast to medium densities, density peaks are present at divertor plates, acting as barriers for fast electrons originating further upstream.

The experimental data from JET divertor Langmuir probes that were available were extensively used for comparisons with the simple model. The comparisons are done in two distinct ways. The first one is plotting the experimental T_e data as a function of the midplane separatrix density in density scan plots for a fixed radial position. The second way is to compare the LP data with T_e from the simple model and EDGE2D-EIRENE for one fixed density case at several radial positions. These comparisons are done in the frame of objective(b)). For the low density regime, the model predicts that probes should measure correctly, and indeed it was confirmed that probe experimental data agree with the EDGE2D-EIRENE prediction for target T_e. However, the comparison with real experimental LP data is particularly important for the medium and high density cases, since this is the region when overestimation of T_e by probes is frequently reported. As stated above, for the high density case, according to our model, the effect of fast electrons is negligible. This suggests that the cause of overestimation may be different than fast electrons (assuming that the shape of the EDGE2D-EIRENE profiles is correct for these cases). This result is also tentatively suggested in [13] for TCV.

It is important to point out that it was also found that the effect of hot electrons on single LP IV characteristics is similar to the sheath expansion effect, which is treated by the 4-parameter fit. As a result, use of the 4-parameter fit itself significantly reduces the effect of hot upstream electrons on T_e deduced by fitting the single LP IV characteristics.

Finally, input data from the kinetic BIT1 code is used to calculate an EVDF by the simple model with the intention to benchmark the simple model against BIT1. It was found that the target EVDFs for the high recycling regime from BIT1 and from the simple model are both non-Maxwellian but qualitatively very similar, both with a significant population of hot electrons at the tail of the EVDF. Both EVDFs also yield similar synthetic probe T_e measurements (objective (c)). BIT1 is a PIC code which uses much more detailed physics and the time to perform one computation of one single parallel profile can take tens of hours on supercomputers. Contrarily, the simple model can calculate the target EVDF in tens of seconds on an ordinary PC. Since agreement between BIT1 and the simple model target EVDF has been found, this suggests that the simple model can be a valuable tool for quick predictions of the form of the target EVDF provided that the input profiles are specified, e.g. by EDGE2D-EIRENE (objective (d)).

List of acronyms

ASDEX Axially Symmetric Divertor Experiment

EFDA European Fusion Development Agreement

ELM Edge Localized Mode

EURATOM European Atomic Energy Community

EVDF Electron Velocity Distribution Function

HRR High recycling regime

IR Infrared

JET Joint European torus

LCFS Last Closed Flux Surface

LP Langmuir Probe

MAST Mega Amper Spherical Tokamak

MHD Magneto-hydrodynamics

NBI Neutral beam injection

PIC Parcticle in Cell

SOL Scrape-off layer

TCV Tokamak à Configuration Variable

TEXTOR Tokamak Experiment for Technology Oriented Research

Bibliography

[1] J. Freidberg, *Plasma physics and fusion energy*, Cambridge university press, Cambridge, 2007.

[2] J. Wesson, *The science of JET*, IoP, 2006.

[3] J. Wesson, *Tokamaks*, Clarendon press, Oxford, 2004.

[4] JET users pages, *http://users.jet.efda.org/*, (cit. 8.4.2014).

[5] EFDA web pages, *http://www.efda.org/fusion*, (cit. 9.4.2014).

[6] *Design Proposal for the Joint European Torus - EUR-JET-R5*, European Comission, Luxembourg, 1973.

[7] P. C. Stangeby *The plasma boundary of magnetic fusion devices*, IoP, 2000.

[8] I. H. Hutchinson, *Principles of plasma diagnostics*, Cambridge University Press, 2002.

[9] Ph. Chappuis et al., *The Design of a New JET Divertor for High Triangularity and High Current Scenarios*, Proceedings of SOFT 2002, Helsinki, Finland, 2002

[10] K. Lackner et al., *Fusion physics*, IAEA, Vienna, 2012

[11] K. Jesko, *Okrajové plazma v tokamacích*, Bakalářská práce, 2012

[12] M. Groth et al., *Impact of Carbon and Tungsten as Divertor Materials on the Scrape-off Layer Conditions in JET*, IAEA Proceedings, preprint, 2012

[13] J. Horáček et al., *Predicted effects of parallel temperature gradients on the overestimation of TCV divertor target Langmuir probe Te measurements*, Journal of Nuclear Materials 313-316 (2003) 931-935.

[14] D. Tskhakaya et al., *Interpretation of divertor Langmuir probe measurements during ELMs at JET*, Journal of Nuclear Materials 415 (2011) 860-864.

[15] P. C. Stangeby, *Correction to Te values measured by a Langmuir probe allowing for weak collisionality of fast electrons*, in preparation

[16] A. Pochelon et al., *Energy confinement and MHD activity in shaped TCV plasmas with localized electron cyclotron heating*, Nuclear Fusion, Vol. 39, No. 11Y (1999) 1807-1818.

[17] J. D. Swift, M. J. Schwarz, *Electric probes for plasma diagnostics*, Elsevier, London, 1969.

[18] G. F. Matthews et al., *Tokamak plasma diagnosis by electrical probes*, Plasma Phys. Control. Fusion 36 (1994) 1595.

[19] R. D. Monk et al., *Interpretation of ion flux and electron temperature profiles at the JET divertor target during high recycling and detached discharges*, Journal of Nuclear Materials 241–243 (1997) 396–401.

[20] G. Fussmann, U. Ditte, W. Eckstein, et al., *Divertor parameters and divertor operation in ASDEX*, Journal of Nuclear Materials 128-129 (1984) 350–358.

[21] J. G. Watkins et al. Comparison of Langmuir probe and Thomson scattering measurements in DIII-D, JNM 290-293 (2001) 778-782.

[22] J. D. Huba, *NRL plasma formulary*, Naval Research Laboratory, 2007.

[23] J. Wesson, *Effect of temperature gradient on plasma sheath*, Plasma Phys. Control. Fusion 37 (1995) 1459.

[24] D. Reiter, M. Baelmans and P. Börner, *The EIRENE and B2-EIRENE codes*, Fusion science and technology vol. 47 (2005) 172-186.

[25] P. Kulhánek, Úvod do teorie plazmatu, AGA, 2013

[26] P. Vondráček, *Studium okrajového plazmatu tokamaku COMPASS pomocí dvojice reciprokých sond* , Diplomová práce, 2012

[27] M. A. Jaworski et al., *Modification of the electron energy distribution function during lithium experiments on the National Spherical Torus Experiment*, Fusion Engineering and Design 87 (2012) 1711– 1718

[28] C. Guillemaut et al., *Influence of atomic physics on EDGE2D-EIRENE simulations of JET divertor detachment with carbon and beryllium/tungsten plasma-facing components*, Doctoral thesis, 2013

[29] R. Dejarnac et al., *Study of ion sheath expansion and anisotropy of the electron parallel energy distribution in the CASTOR tokamak*, Plasma Phys. Control. Fusion 49 (2007) 1791

[30] P. C. Stangeby and G. M. McCracken 1990 Nucl. Fusion 30 1232

[31] J. Wesson, *Effect of temperature gradient on plasma sheath*, Plasma Phys. Control. Fusion 37 (1995) 1459-146

[32] P. C. Stangeby, *A problem in the interpretation of tokamak Langmuir probes when a fast electron component is present*, Plasma Phys. Control. Fusion 37 (1995) 1031-1037

[33] T. K. Popov et al., *Electron energy distribution function, plasma potential and electron density measured by Langmuir probe in tokamak edge plasma.*, Plasma Phys. Control. Fusion 51 (2009) 065014 (15pp)

[34] T. J. M. Boyd, J. J. Sanderson., *The Physics of Plasmas.*, Cambridge University Press